

The kinematics of the reduced velocity gradient tensor in a fully developed turbulent free shear flow

P. K. Rabey¹, A. Wynn¹ and O. R. H. Buxton^{1,†}

¹Department of Aeronautics, Imperial College London, London, SW7 2AZ, UK

(Received 31 July 2014; revised 15 January 2015; accepted 26 January 2015;
first published online 20 February 2015)

This paper examines the kinematic behaviour of the reduced velocity gradient tensor (VGT), \tilde{A}_{ij} , which is defined as a 2×2 block, from a single interrogation plane, of the full VGT $A_{ij} = \partial u_i / \partial x_j$. Direct numerical simulation data from the fully developed turbulent region of a nominally two-dimensional mixing layer are used in order to examine the extent to which information on the full VGT can be derived from the reduced VGT. It is shown that the reduced VGT is able to reveal significantly more information about regions of the flow in which strain rate is dominant over rotation. It is thus possible to use the assumptions of homogeneity and isotropy to place bounds on the first two statistical moments (and their covariance) of the eigenvalues of the reduced strain-rate tensor (the symmetric part of the reduced VGT) which in turn relate to the turbulent strain rates. These bounds are shown to be dependent upon the kurtosis of $\partial u_1 / \partial x_1$ and another variable defined from the constituents of the reduced VGT. The kurtosis is observed to be minimised on the centreline of the mixing layer and thus tighter bounds are possible at the centre of the mixing layer than at the periphery. Nevertheless, these bounds are observed to hold for the entirety of the mixing layer, despite departures from local isotropy. The interrogation plane from which the reduced VGT is formed is observed not to affect the joint probability density functions (p.d.f.s) between the strain-rate eigenvalues and the reduced strain-rate eigenvalues despite the fact that this shear flow has a significant mean shear in the cross-stream direction. Further, it is found that the projection of the eigenframe of the strain-rate tensor onto the interrogation plane of the reduced VGT is also independent of the plane that is chosen, validating the approach of bounding the full VGT using the assumption of local isotropy.

Key words: shear layer turbulence, turbulence control, turbulence theory

1. Introduction

The fine scales of turbulence are primarily characterised by the velocity gradient tensor (VGT), which can be split into a symmetric and skew-symmetric tensor as follows:

$$A_{ij} = \frac{\partial u_i}{\partial x_j} = S_{ij} + \Omega_{ij} = \frac{1}{2} \left(\frac{\partial u_i}{\partial x_j} + \frac{\partial u_j}{\partial x_i} \right) + \frac{1}{2} \left(\frac{\partial u_i}{\partial x_j} - \frac{\partial u_j}{\partial x_i} \right), \quad (1.1)$$

† Email address for correspondence: o.buxton@imperial.ac.uk

with the scalar analogues to strain rate (S_{ij}) and rotation (Ω_{ij}) being dissipation (ϵ) and enstrophy (ω^2) respectively. In the Richardson–Kolmogorov phenomenology the dissipative (Kolmogorov) length scale is defined from the mean rate of dissipation within a flow and thus the VGT can be considered to provide one of the few rigid definitions of ‘scales’ within the energy cascade (Tsinober 2009). The fluctuation of enstrophy is a characterising feature of turbulent flows (Tennekes & Lumley 1972) and it is used, for example, as a threshold quantity to distinguish between turbulent and non-turbulent fluid in free shear flows, e.g. Bisset, Hunt & Rogers (2002) and da Silva & Pereira (2008). For further details an excellent review of the phenomena of the VGT can be found in Meneveau (2011).

The Navier–Stokes equations can be re-formulated to reveal the dynamics of the strain-rate tensor and the rotation tensor as follows:

$$\frac{1}{2} \frac{D(S_{ij}S_{ij})}{Dt} = -S_{ij}S_{jk}S_{ki} - \frac{1}{4}\omega_i S_{ij}\omega_j - S_{ij} \frac{\partial^2 p}{\partial x_i \partial x_j} + \nu S_{ij} \nabla^2 S_{ij}, \quad (1.2)$$

$$\frac{1}{2} \frac{D\omega^2}{Dt} = \omega_i S_{ij}\omega_j + \nu \omega_i \nabla^2 \omega_i, \quad (1.3)$$

where $-S_{ij}S_{jk}S_{ki}$ and $\omega_i S_{ij}\omega_j$, the self-amplification of strain rate and the amplification of enstrophy by vortex stretching respectively, are the inviscid source/sink terms derived from the VGT. The term $\omega_i S_{ij}\omega_j$, in particular, has been studied extensively since the observation of Taylor (1938a) that $\langle \omega_i S_{ij}\omega_j \rangle > 0$ for turbulent flows, where $\langle \cdot \rangle$ denotes ensemble averaging. This mean increase in enstrophy by vortex stretching is the only known mechanism by which energy is transferred from large scales to small scales within the energy cascade and prompted Tsinober (2009) to state that without $\langle \omega_i S_{ij}\omega_j \rangle > 0$ three-dimensional turbulence could not exist. This term is representative of the interaction between strain and rotation within turbulence which despite being often weak and non-local (Tsinober, Shtilman & Vaisburd 1997) is observed to be highly intermittent in a variety of turbulent flows (Betchov 1975; Tsinober, Kit & Dracos 1992). This term, and hence the interaction between strain rate and rotation, can further be written as (Betchov 1956)

$$\omega_i S_{ij}\omega_j = \omega^2 s_i (\hat{e}_i \cdot \hat{\omega})^2, \quad (1.4)$$

where s_i are the (three) eigenvalues of S_{ij} with corresponding eigenvectors e_i , $\hat{\cdot}$ implies a unit vector and repetition of the subscript i implies summation.

The strain-rate eigenvalues s_i can be ordered such that $s_1 \geq s_2 \geq s_3$ with $s_1 \geq 0$ (extensive) and $s_3 \leq 0$ (compressive). Continuity for an incompressible fluid requires that $s_1 + s_2 + s_3 = 0$ and thus the intermediate eigenvalue, s_2 , is either mildly extensive or compressive but bounded by the magnitudes of s_1 and s_3 . In this way Betchov (1956) explains that the topological evolution of a fluid element is determined by the sign of s_2 , with $s_2 > 0$ implying two orthogonal extensive strain rates and a further orthogonal compressive strain rate leading to the formation of ‘sheet-like structures’ and $s_2 < 0$ implying two orthogonal compressive strain rates in conjunction with a further orthogonal extensive strain rate leading to the formation of ‘tube-like’ structures. It has since been observed that the interaction between strain rate and rotation is characterised by a surprising (considering that $\langle \omega_i S_{ij}\omega_j \rangle > 0$) preferential parallel alignment between the vorticity vector and the intermediate strain-rate eigenvector, i.e. $(\hat{e}_2 \cdot \hat{\omega})^2 \approx 1$ in (1.4) (Ashurst *et al.* 1987; Tsinober *et al.* 1992; Tanahashi, Iwase & Miyauchi 2001; Mullin & Dahm 2006), although

it has subsequently been shown that the $(\hat{e}_1 \cdot \hat{\omega})^2$ alignment is more significant in determining the sign of $\omega_i S_{ij} \omega_j$ (Buxton & Ganapathisubramani 2010).

A full topological classification of the flow, defined in terms of the strain rate and rotation and their inviscid source/sink terms, can be achieved by examination of the invariants of the characteristic equation for the VGT (Chong, Perry & Cantwell 1990):

$$\lambda^3 + P\lambda^2 + Q\lambda + R = 0. \quad (1.5)$$

The first invariant is equal to the negative of the trace of the VGT ($P = -A_{ii}$) which is equivalent to the divergence of the flow field and is thus zero for an incompressible flow. The state of fluid elements within a turbulent flow is thus described by the second invariant $Q = (\|\Omega_{ij}\|^2 - \|S_{ij}\|^2)/2$, which represents the local excess of rotation over strain rate, and the third invariant R , which is defined as the negative of the determinant of A_{ij} , thus $R = (-S_{ij}S_{jk}S_{ki} - (3/4)\omega_i S_{ij} \omega_j)/3$ is the local excess of self-amplification of strain rate over amplification of enstrophy. In P - Q - R space the discriminant surface that separates purely real roots to (1.5) from one real root and a complex-conjugate pair of roots is

$$27R^2 + (4P^3 - 18PQ)R + (4Q^3 - P^2Q^2) = 0 \quad (1.6)$$

and thus for incompressible flows ($P = 0$) the discriminant can be given by $\Delta = Q^3 + (27/4)R^2$. When $\Delta < 0$ only real eigenvalues exist and the flow is purely straining whereas when $\Delta > 0$ the fluid is swirling (Perry & Chong 1994). The joint probability density function (p.d.f.) of the second and third invariants produces a distinct, characteristic ‘tear drop’ shape which is considered to be ‘universal’ for fully developed turbulent flows (Elsinga & Marusic 2010). The line for $\Delta = 0$ acts as an attractor, giving the ‘Vieillefosse tail’ (Vieillefosse 1982) which can be seen in the bottom right quadrant of figure 1.

Invariants can also be computed for the strain-rate and rotation tensors individually. For an incompressible flow both tensors have zero trace (the rotation tensor is skew symmetric and thus has no trace by definition), hence $P_S = -S_{ii} = -A_{ii} = 0$ and $P_\Omega = -\Omega_{ii} = 0$ and the determinant of the rotation tensor is zero meaning that $R_\Omega = 0$. The remaining invariants are given by $Q_S = -(S_{ij}S_{ij})/2$, $R_S = -(S_{ij}S_{jk}S_{ki})/3$ and $Q_\Omega = (\Omega_{ij}\Omega_{ij})/2$ (the strain or rotation parts of the invariants of the VGT). The second strain-rate and rotation matrix invariants are given physical meaning in the following equations:

$$\epsilon = 2\nu S_{ij}S_{ij} = -4\nu Q_S \quad (1.7)$$

$$\phi = -\frac{1}{4}\Omega_{ij}\Omega_{ij} = \frac{1}{2}Q_\Omega, \quad (1.8)$$

where ϵ is the dissipation of kinetic energy due to viscous friction and ϕ is the enstrophy density (Perry & Chong 1994).

Despite the wealth of information that can be extracted from the VGT in a developed turbulent flow it is only relatively recently that experimental techniques, such as holographic particle image velocimetry (PIV) (Zhang, Tao & Katz 1997) or tomographic PIV (Elsinga *et al.* 2006) have developed the capability to produce the three-dimensional, three-component (3D3C) data that are required. However, limitations in the spatial resolution and signal to noise ratio for these techniques are still a significant hindrance to studying the kinematics of the VGT. Additionally, it is not possible to acquire 3D3C data in real time with present technology levels (either experimentally or numerically). Thus to formulate a model of the VGT, that can act

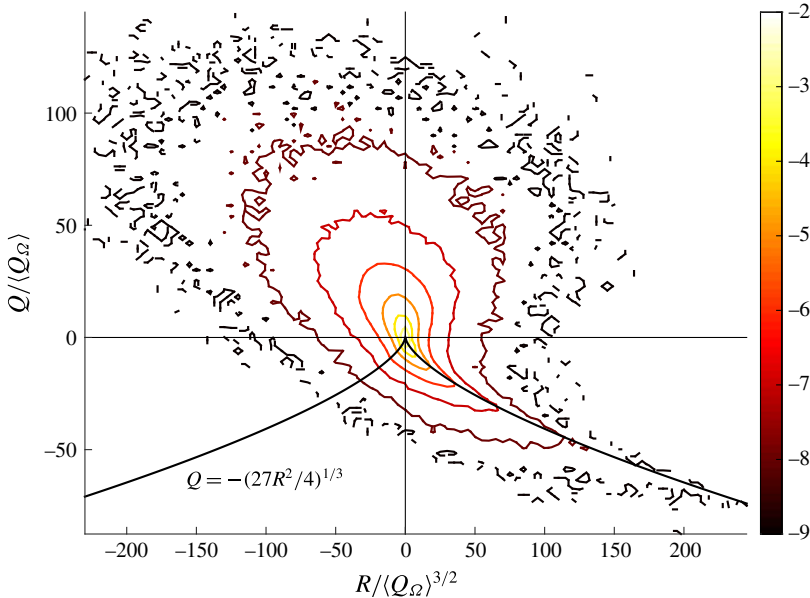


FIGURE 1. (Colour online) Joint probability density function (p.d.f.) between Q and R for the mixing layer data of the present study. Contours scale logarithmically. The ‘teardrop’ shape is considered to be a ‘universal’ property for all fully developed turbulent flows.

as the observed state in a closed-loop feedback controller to ‘control’ velocity gradient phenomena (such as dissipation, for example) it is necessary to place bounds upon such phenomena from 2D2C data which can be acquired in real time. An example of an experiment capable of acquiring such data would be two offset ‘X-wire’ CTA (constant temperature anemometry) probes used in conjunction with Taylor’s frozen flow field hypothesis (Taylor 1938*b*). For these reasons Cardesa *et al.* (2013) explored the invariants of the reduced VGT, \tilde{A}_{ij} , which is defined as a 2×2 matrix extracted from the full VGT, and is thus comprised of 2D2C data that are readily obtainable in a laboratory experiment. For convenience Cardesa *et al.* (2013) consider the upper left 2×2 block of the full VGT (velocity components u_1 and u_2 in the x_1 – x_2 plane).

Using an approach in which 2D2C data were used to describe three-dimensional topological features of high-Reynolds-number, fine-scale turbulence, the recently published study of Fiscoletti, Westerweel & Elsinga (2014) made use of the reduced VGT to demonstrate the topology of intense dissipation and enstrophy in a high-Reynolds-number ($Re_\lambda = 349$) axisymmetric jet with excellent spatial resolution. They made use of microscopic, planar PIV experiments (purely two-dimensional data) to show the tendency for regions of high dissipation to be distributed as sheet-like structures surrounding the perimeter of high-entrophy tubes at a characteristic offset that scales with the Kolmogorov length scale. These results are in agreement with the scalings derived in much lower Reynolds number 3D3C simulations/experiments (e.g. Jiménez *et al.* 1993 and Mullin & Dahm 2006) and thus demonstrate the capability to infer fully three-dimensional topological velocity gradient information from the reduced VGT.

The characteristic equation for the reduced VGT is given as

$$\lambda^2 + p\lambda + q = 0, \quad (1.9)$$

where p and q are the first and second invariants respectively. Unlike its 3D counterpart, the first invariant of the reduced VGT, $p = -\text{tr}(\tilde{\mathbf{A}})$, is usually non-zero in an incompressible flow (if $\text{tr}(\mathbf{A}_{ij}) = 0$, $\text{tr}(\tilde{\mathbf{A}}_{ij}) = 0$ only when $A_{33} = 0$) and so the 2D projection of an incompressible 3D flow appears compressible. The invariant p determines the stability of the flow locally, with regions for which $p < 0$ being unstable when perturbed (Perry & Chong 1987). The second invariant is computed as $q = \det(\tilde{\mathbf{A}})$. Cardesa *et al.* (2013) showed that the joint p.d.f. of the invariants of the reduced VGT has been found to also produce a characteristic ‘teapot’ shape for a number of turbulent flows, with the discriminant $\tilde{\Delta} = (p^2 - q)/4 = 0$ also acting as an attractor, as in the 3D case. When $\tilde{\Delta} > 0$ the reduced system has two real, distinct eigenvalues and critical points in the flow will produce nodes or saddles; whilst when $\tilde{\Delta} < 0$ they will form foci (Perry & Chong 1987).

Cardesa *et al.* (2013) were able to derive a number of important statistical results by using the assumption of local homogeneity, namely they showed that $\langle p \rangle = 0$ and $\langle q \rangle = 0$. Further, they are able to show that $\langle pq \rangle < 0$ which is shown to follow mathematically from the observation that $\langle \omega_i \mathcal{S}_{ij} \omega_j \rangle > 0$ since under the further assumption of local isotropy $\langle pq \rangle = -\langle \omega_i \mathcal{S}_{ij} \omega_j \rangle / 15$. Finally, by consideration of the eigenvalues of the reduced strain-rate tensor (\tilde{s}_i) they are able to show that for a limited number of points within the flow, namely $\tilde{s}_1 > \tilde{s}_2 > 0$ and $\tilde{s}_2 < \tilde{s}_1 < 0$ then the sign of the intermediate strain-rate eigenvalue (s_2) can be inferred and thus whether the fluid is undergoing ‘sheet-forming’ or ‘tube-forming’ topological evolution. This manuscript makes further progress by seeking more rigid bounds on 3D VGT quantities, such as s_2 , from their counterparts in the reduced VGT. Additionally the instantaneous variation of these VGT quantities with their 3D VGT counterparts will be considered as this is a vital step in the formulation of a model of the VGT to close the feedback loop in which the reduced VGT plays the role of the observed state.

2. Invariants of the full and reduced VGT

By using the assumptions of homogeneity and local isotropy Cardesa *et al.* (2013) were able to derive the following relations:

$$\langle pq \rangle = \frac{7}{6} \langle p^3 \rangle, \quad (2.1)$$

$$\langle pq \rangle = -\frac{1}{15} \langle \omega_i \mathcal{S}_{ij} \omega_j \rangle. \quad (2.2)$$

We follow the convention of Cardesa *et al.* (2013) and choose to define the reduced VGT as the upper left-hand 2×2 block of the VGT, i.e. gradients of u_1 and u_2 in the x_1 – x_2 plane. This choice is arbitrary and we subsequently discuss the choice of the interrogation plane for the formation of the VGT in § 7. The invariants of the reduced VGT can thus be expressed as $p = -\text{tr}(\tilde{\mathbf{A}}_{ij}) = -(A_{11} + A_{22})$ and $q = \det(\tilde{\mathbf{A}}_{ij}) = A_{11}A_{22} - A_{12}A_{21}$. Rewriting the second and third invariants of the full VGT, Q and R respectively, we thus obtain

$$Q = -p^2 + q - (A_{13}A_{31} + A_{23}A_{32}), \quad (2.3)$$

$$R = -pq + (A_{11}A_{23}A_{32} + A_{22}A_{13}A_{31}) - (A_{12}A_{23}A_{31} + A_{13}A_{32}A_{21}). \quad (2.4)$$

It is observed that the second invariant, Q , can be decomposed into a component containing entries from only the reduced VGT and further terms that cannot be deduced from the reduced VGT alone. Here Q is physically interpreted as the

local excess of rotation over strain rate and is mathematically expressed as double velocity gradient products which can be observed in a two-dimensional projection of turbulence. However, p is a residual of the fact that the projection of an incompressible three-dimensional velocity field onto a two-dimensional subspace appears compressible, i.e. the reduced VGT has a non-zero trace excepting the trivial case of $\partial u_z/\partial z = 0$, where z is the out of plane direction with respect to the reduced VGT source plane. Contrastingly q , a difference between the normal and transverse velocity gradients in the source plane of the reduced VGT, is thus more physically meaningful than p . This is demonstrated in §5 in which we compare the distributions of Q against p and q to a test case flow consisting of the fully developed region of a nominally two-dimensional mixing layer, described in §4.

R , on the other hand, is a sum of triple velocity gradient products and reveals the local excess of inviscid strain-rate amplification over enstrophy amplification. These terms are not present in the dynamics of two-dimensional turbulence, with the only mechanism by which enstrophy changes in time being via the direct action of viscosity (Batchelor 1969). This is reflected in (2.4) in which no decoupling of the terms of the reduced VGT and those not captured in the reduced VGT is possible with the exception of the first term, $-pq$, the mean of which is shown to predict $\langle \omega_i \mathcal{S}_{ij} \omega_j \rangle$ under the assumption of isotropy in (2.2).

3. Relationship between the full and reduced strain-rate tensors

We now re-write the strain-rate tensor, \mathcal{S}_{ij} , as

$$\mathcal{S}_{ij} := \begin{pmatrix} A_{11} & D_{12} & D_{13} \\ D_{12} & A_{22} & D_{23} \\ D_{13} & D_{23} & -(A_{11} + A_{22}) \end{pmatrix} \quad (3.1)$$

and, following Cardesa *et al.* (2013), the reduced strain-rate tensor $\tilde{\mathcal{S}}_{ij}$ is taken to be the upper-left 2×2 block of \mathcal{S}_{ij} , that is,

$$\tilde{\mathcal{S}}_{ij} := \begin{pmatrix} A_{11} & D_{12} \\ D_{12} & A_{22} \end{pmatrix}. \quad (3.2)$$

Recall that the eigenvalues of \mathcal{S}_{ij} are denoted s_i (with corresponding eigenvectors \mathbf{e}_i) and are assumed to be ordered $s_1 \geq s_2 \geq s_3$, while the eigenvalues \tilde{s}_i (and corresponding eigenvectors $\tilde{\mathbf{e}}_i$) of the reduced strain-rate tensor $\tilde{\mathcal{S}}_{ij}$ are assumed to satisfy $\tilde{s}_1 \geq \tilde{s}_2$, although no strict sign condition may be placed upon them. The purpose of this section is to discuss to what extent information on the eigenvalues/eigenvectors of \mathcal{S}_{ij} can be determined, given that $\tilde{\mathcal{S}}_{ij}$ is known.

3.1. Eigenvalue bounds

Cardesa *et al.* (2013) showed that the sign of the intermediate eigenvalue s_2 can be determined when the two reduced eigenvalues have the same sign: if $0 < \tilde{s}_2 \leq \tilde{s}_1$, then $s_2 > 0$; while if $\tilde{s}_2 \leq \tilde{s}_1 < 0$ it follows that $s_2 < 0$. Whilst interesting from the point of view that the sign of s_2 determines whether the flow is locally ‘sheet-forming’ or ‘tube-forming’, such a result does not place any bounds upon the magnitude of s_2 , nor give any information regarding the remaining eigenvalues s_1, s_3 .

To provide such information, observe that since S_{ij} is symmetric it follows from Horn & Johnson (2013, Theorem 4.3.17), that the eigenvalues of the two matrices are ‘interlaced’, namely,

$$s_3 \leq \tilde{s}_2 \leq s_2 \leq \tilde{s}_1 \leq s_1. \quad (3.3)$$

It is immediate that the result of Cardesa *et al.* (2013) follows from the central pair of inequalities $\tilde{s}_2 \leq s_2 \leq \tilde{s}_1$. Interestingly, (3.3) requires only the fact that S_{ij} is symmetric, whereas the proof presented in Cardesa *et al.* (2013) requires the assumption of incompressibility. Furthermore, in addition to determining the sign of s_2 , (3.3) now enables bounds to be placed upon the remaining eigenvalues of S_{ij} .

If we additionally assume that the flow is incompressible we can show that

$$k_i S_{ij} k_j = A_{33} = -(A_{11} + A_{22}) = \tilde{S}_{ii} = -(\tilde{s}_1 + \tilde{s}_2), \quad (3.4)$$

where k is a unit vector in the x_3 direction. Now, the Rayleigh–Ritz theorem (Horn & Johnson 2013) states that the maximum and minimum eigenvalues of S_{ij} provide upper and lower bounds for the quantity $\sup\{v_i S_{ij} v_j : v^2 = 1\}$. Consequently,

$$s_3 \leq -(\tilde{s}_1 + \tilde{s}_2) \leq s_1. \quad (3.5)$$

Combining (3.3) and (3.5), we can infer the following information regarding the eigenvalues of S_{ij} from the reduced strain-rate tensor \tilde{S}_{ij} :

$$s_3 \leq \min\{\tilde{s}_2, -(\tilde{s}_1 + \tilde{s}_2)\}, \quad \tilde{s}_2 \leq s_2 \leq \tilde{s}_1, \quad \max\{\tilde{s}_1, -(\tilde{s}_1 + \tilde{s}_2)\} \leq s_1. \quad (3.6a-c)$$

Hence, incompressibility provides an improved bound on s_3 when $2\tilde{s}_2 + \tilde{s}_1 > 0$, and an improved bound upon s_1 when $2\tilde{s}_1 + \tilde{s}_2 < 0$. We now derive asymmetric bounds such that, for example, if $\tilde{s}_1 < 0$ then, by (3.6), $s_1 \geq -(\tilde{s}_1 + \tilde{s}_2) \geq -2\tilde{s}_1$. These bounds, which are specific examples of the more general (3.6), are summarised as follows:

$$\left. \begin{aligned} s_1 &\geq -2\tilde{s}_1|_{\tilde{s}_1 < 0}, & s_1 &\geq -\frac{1}{2}\tilde{s}_2|_{\tilde{s}_2 < 0}, \\ s_3 &\leq -\frac{1}{2}\tilde{s}_1|_{\tilde{s}_1 > 0}, & s_3 &\leq -2\tilde{s}_2|_{\tilde{s}_2 > 0}. \end{aligned} \right\} \quad (3.7)$$

It is important to emphasise that the bounds on the eigenvalues shown in (3.6) were proven using only the facts that S_{ij} is symmetric and trace-free, that is, that the velocities were sampled from an incompressible flow. It is only the particular form of the distributions within these bounds which captures the intricacies of the flow physics.

3.2. Invariants of the full and reduced strain-rate tensor

As discussed in §1, the invariants $Q = (\|\Omega_{ij}\| - \|S_{ij}\|)/2$ and $R = (S_{ij}S_{jk}S_{ki} - (3/4)\omega_i S_{ij} \omega_j)/3$ of the VGT are convenient tools with which to describe the instantaneous flow topology. Since the invariants of the strain-rate tensor are given by

$$Q_S = -\frac{1}{2}S_{ij}S_{ij}, \quad R_S = -\frac{1}{3}S_{ij}S_{jk}S_{ki}, \quad (3.8a,b)$$

it is clear that evaluating these invariants has direct implications for the behaviour of the full VGT. Furthermore, the first reduced strain-rate invariant determines the dissipation of kinetic energy due to viscous friction as illustrated in (1.7).

It is therefore of interest to discuss the extent to which Q_S and R_S can be estimated, given that the reduced strain-rate tensor \tilde{S}_{ij} is known. Analogously to the VGT,

the reduced invariants of \tilde{S}_{ij} are defined to be the coefficients of its characteristic polynomial

$$p_S = -(A_{11} + A_{22}) = -(\tilde{s}_1 + \tilde{s}_2), \quad q_S = A_{11}A_{22} - D_{12}^2 = \tilde{s}_1\tilde{s}_2. \tag{3.9a,b}$$

Since the full invariants can be expressed in terms of the eigenvalues of S_{ij} as

$$\left. \begin{aligned} Q_S &= s_1s_2 + s_1s_3 + s_2s_3, \\ R_S &= -s_1s_2s_3, \end{aligned} \right\} \tag{3.10}$$

it appears that Q_S and q_S are likely to be most closely related. Indeed, the bounds identified in (3.6) allow Q_S to be estimated in terms of q_S .

To this end, suppose first that $q_S \leq 0$. Then, by (3.6), $s_3 \leq \tilde{s}_2 \leq 0 \leq \tilde{s}_1 \leq s_1$ and it follows that $s_1s_3 \leq \tilde{s}_1\tilde{s}_2$. Assuming incompressibility,

$$Q_S = s_1s_3 + (s_1 + s_3)s_2 = s_1s_3 - s_2^2 \leq \tilde{s}_1\tilde{s}_2 = q_S. \tag{3.11}$$

Next, suppose that $q_S > 0$. This occurs if either $\tilde{s}_1 \geq \tilde{s}_2 > 0$ or $\tilde{s}_2 \leq \tilde{s}_1 < 0$. In the former case, $s_3 = -(s_1 + s_2)$ can substituted into (3.10) to show that

$$Q_S = -3s_1s_2 - (s_1 - s_2)^2 \leq -3s_1s_2 \leq -3\tilde{s}_1\tilde{s}_2 = -3q_S, \tag{3.12}$$

where the final inequality follows from (3.6). In the latter, a similar argument provides that same bound:

$$Q_S = -3s_2s_3 - (s_2 - s_3)^2 \leq -3s_2s_3 \leq -3\tilde{s}_1\tilde{s}_2 = -3q_S. \tag{3.13}$$

In summary,

$$Q_S \leq \begin{cases} q_S & \text{for } q_S \leq 0, \\ -3q_S & \text{for } q_S > 0. \end{cases} \tag{3.14}$$

3.3. Statistics of the reduced strain-rate tensor

In §§ 3.1 and 3.2 it has been shown that, as a consequence of incompressibility, bounds can be placed upon the invariants and eigenvalues of S_{ij} based only upon knowledge of \tilde{S}_{ij} . However, to determine how often these bounds can provide useful information, it is of interest to understand the statistics of the reduced eigenvalues.

For example, to infer from (3.6) that the flow is either ‘tube-forming’ or ‘sheet-forming’ requires $\tilde{s}_1 < 0$ or $\tilde{s}_2 > 0$, respectively, and it was noted in Cardesa *et al.* (2013) that such situations occur in approximately 14.2% of the studied data ensemble. However, currently, the only known statistical information is that $\langle \tilde{s}_1 \rangle = -\langle \tilde{s}_2 \rangle$ and that $\langle \tilde{s}_1\tilde{s}_2 \rangle = -(5/4)\langle (\partial u_1/\partial x_1)^2 \rangle$. Under the assumptions of homogeneous and isotropic turbulence, we now extend these results.

3.3.1. Expectation of \tilde{s}_1, \tilde{s}_2

A direct computation gives

$$\tilde{s}_{1,2} = -\frac{p_S}{2} \pm \frac{1}{2}\sqrt{p_S^2 - 4q_S} \tag{3.15}$$

and since $\langle p_s \rangle = \langle p \rangle = 0$, it follows that

$$\langle \tilde{s}_{1,2} \rangle = \pm \frac{1}{2} \left\langle \sqrt{(A_{11} - A_{22})^2 + 4D_{12}^2} \right\rangle = \pm \frac{1}{2} \langle X^{1/2} \rangle. \quad (3.16)$$

Here, we have defined the positive variable $X = (A_{11} - A_{22})^2 + 4D_{12}^2 = p_s^2 - 4q_s$.

Evaluating the expected value of the square root of X directly is difficult. However, X depends only upon terms in the symmetric strain-rate tensor. Therefore, under the assumption of isotropy and homogeneity, its moments can be expressed in terms of the moments of $\partial u_1 / \partial x_1$ (Hierro & Dopazo 2003). Indeed, we obtain

$$\langle X \rangle = 6 \left\langle \left(\frac{\partial u_1}{\partial x_1} \right)^2 \right\rangle, \quad \langle X^2 \rangle = 24 \left\langle \left(\frac{\partial u_1}{\partial x_1} \right)^4 \right\rangle. \quad (3.17a,b)$$

This information can be used to estimate $\langle X^{1/2} \rangle$.

First, the Cauchy–Schwarz inequality implies that $\langle X^{1/2} \rangle \leq \langle X \rangle^{1/2}$. Next, suppose that constants $a, b > 0$ are chosen such that $x^{1/2} \geq -ax^2 + bx$, for all $x \geq 0$. Then it is shown in appendix A that

$$\langle X^{1/2} \rangle \geq \langle X \rangle^{1/2} \left(b - a \frac{\langle X^2 \rangle}{\langle X \rangle^2} \right). \quad (3.18)$$

Hence, using (3.16) and (3.17),

$$\sqrt{\frac{3}{2}} \left\langle \left(\frac{\partial u_1}{\partial x_1} \right)^2 \right\rangle^{1/2} \left(b - \frac{2a\kappa}{3} \right) \leq \langle \tilde{s}_1 \rangle \leq \sqrt{\frac{3}{2}} \left\langle \left(\frac{\partial u_1}{\partial x_1} \right)^2 \right\rangle^{1/2}, \quad (3.19)$$

where $\kappa := \langle (\partial u_1 / \partial x_1)^4 \rangle / \langle (\partial u_1 / \partial x_1)^2 \rangle^2$ is the kurtosis of $\partial u_1 / \partial x_1$.

It is clear that the lower bound in (3.19) is only meaningful if $c(a, b) := b - 2a\kappa/3 > 0$, and that a larger value of this constant provides a tighter estimate of $\langle \tilde{s}_1 \rangle$. Consequently, we should aim to maximize $c(a, b)$ subject to the constraint $x^{1/2} \geq -ax^2 + bx$, for all $x \geq 0$. It is shown in appendix A that the solution to this constrained optimisation problem is $c_{max} = \sqrt{3/2\kappa}$. Hence,

$$\sqrt{\frac{3}{2\kappa}} \leq \frac{\langle \tilde{s}_1 \rangle}{\sqrt{\frac{3}{2}} \left\langle \left(\frac{\partial u_1}{\partial x_1} \right)^2 \right\rangle^{1/2}} \leq 1 \quad (3.20)$$

and since $\langle \tilde{s}_2 \rangle = -\langle \tilde{s}_1 \rangle$,

$$-1 \leq \frac{\langle \tilde{s}_2 \rangle}{\sqrt{\frac{3}{2}} \left\langle \left(\frac{\partial u_1}{\partial x_1} \right)^2 \right\rangle^{1/2}} \leq -\sqrt{\frac{3}{2\kappa}}. \quad (3.21)$$

The estimates (3.20) and (3.21) agree with and extend the previously proven (Cardesa *et al.* 2013) result that, assuming isotropy and homogeneity, $\langle \tilde{s}_2 \rangle = -\langle \tilde{s}_1 \rangle \leq 0 \leq \langle \tilde{s}_1 \rangle$.

Figure 2 shows the kurtosis (κ) profile of A_{11} throughout the mixing layer data we introduce in § 4. The study of Van Atta & Antonia (1980) compiles the experimental

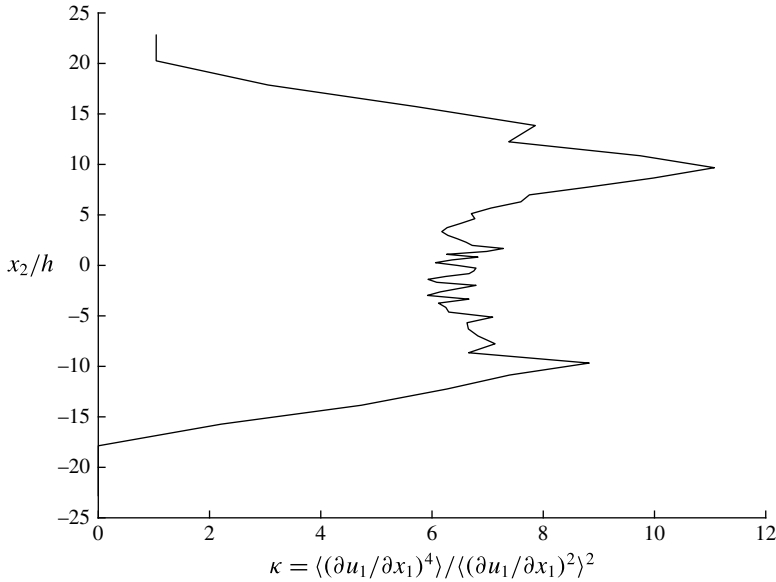


FIGURE 2. Profile of $\kappa(x_2)$.

variation of κ for a variety of different turbulent flows over a range of turbulent Reynolds numbers, Re_λ . They show that in the range $10^2 < Re_\lambda < 10^3$ κ varies as $\kappa \sim Re_\lambda^m$, where m is roughly bounded by $0.32 \lesssim m \lesssim 0.41$. For a nominally two-dimensional free shear flow, such as the mixing layer data, Re_λ is evidently a function of x_2 requiring κ to be a function of x_2 as illustrated in the figure. The value of κ at $x_2 = 0$ of 6.3 compares favourably to that for the mixing layer of Wyngaard & Tennekes (1970) (6.0 ± 0.2) at a comparable $Re_\lambda \approx 300$ for the data introduced in § 4. It should be noted that since κ is minimised at the centreline of the mixing layer (excluding the free stream) the bounding of $\langle \tilde{s}_i \rangle$ is at its narrowest on the centreline and increases towards the peripheries of the mixing layer.

3.3.2. Variance of \tilde{s}_1, \tilde{s}_2

To estimate the variance of the reduced eigenvalues, we first consider their second moments, again assuming isotropy and homogeneity. Using (3.15),

$$\tilde{s}_{1,2}^2 = \frac{1}{4}(p_S^2 + X) \mp \frac{1}{2}p_S\sqrt{X}. \tag{3.22}$$

Now $\langle p_S^2 \rangle = \langle A_{11}^2 + A_{22}^2 + 2A_{11}A_{22} \rangle$ and using the result for double products of velocity derivatives under the assumption of homogeneous isotropic turbulence

$$\left\langle \frac{\partial u_i}{\partial x_l} \frac{\partial u_j}{\partial x_k} \right\rangle = \left[2\delta_{ij}\delta_{kl} - \frac{1}{2}(\delta_{jk}\delta_{il} + \delta_{ik}\delta_{jl}) \right] \left\langle \left(\frac{\partial u_1}{\partial x_1} \right)^2 \right\rangle, \tag{3.23}$$

we obtain $\langle p_S^2 \rangle = \langle (\partial u_1 / \partial x_1)^2 \rangle$. Hence, using (3.17),

$$\langle \tilde{s}_{1,2}^2 \rangle = \frac{7}{4} \left\langle \left(\frac{\partial u_1}{\partial x_1} \right)^2 \right\rangle \mp \frac{1}{2} \langle p_S \sqrt{X} \rangle \tag{3.24}$$

and since $\langle \tilde{s}_1 \rangle = -\langle \tilde{s}_2 \rangle$, the variances of the reduced eigenvalues are related by

$$\sigma_{\tilde{s}_1}^2 - \sigma_{\tilde{s}_2}^2 = -\langle p_S \sqrt{X} \rangle. \tag{3.25}$$

Therefore, the sign of $\langle p_S \sqrt{X} \rangle$ determines which of the reduced eigenvalues has the greater variance. Furthermore, the bounds of (3.20), (3.21) and (3.24) can be used to show that the variances are upper bounded by

$$\frac{\sigma_{\tilde{s}_{1,2}}^2}{\left\langle \left(\frac{\partial u_1}{\partial x_1} \right)^2 \right\rangle} \leq \frac{1}{4} \left(7 - \frac{9}{\kappa} \mp 2 \langle p_S \sqrt{X} \rangle / \left\langle \left(\frac{\partial u_1}{\partial x_1} \right)^2 \right\rangle \right). \tag{3.26}$$

Unfortunately, at present, we are unable to analytically determine the sign of $\langle p_S \sqrt{X} \rangle$. However, since \sqrt{X} is positive and p_S is zero-mean and negatively skewed, we conjecture that $\langle p_S \sqrt{X} \rangle > 0$ and, more specifically, that

$$\frac{\langle p_S \sqrt{X} \rangle}{\left\langle \left(\frac{\partial u_1}{\partial x_1} \right)^2 \right\rangle} = \frac{1}{2}, \tag{3.27}$$

which is supported by its numerical value of 0.50 in the mixing layer data of § 4.

Finally, since $\langle \tilde{s}_1 \tilde{s}_2 \rangle = -(5/4) \langle (\partial u_1 / \partial x_1)^2 \rangle$, the bound of (3.20) can be used to estimate the covariance $\sigma(\tilde{s}_1, \tilde{s}_2) = \langle \tilde{s}_1 \tilde{s}_2 \rangle - \langle \tilde{s}_1 \rangle \langle \tilde{s}_2 \rangle$ of the reduced eigenvalues:

$$\frac{1}{4} \left(\frac{9}{\kappa} - 5 \right) \leq \frac{\sigma(\tilde{s}_1, \tilde{s}_2)}{\left\langle \left(\frac{\partial u_1}{\partial x_1} \right)^2 \right\rangle} \leq \frac{1}{4}. \tag{3.28}$$

The fact that the above bound is asymmetric about zero is suggestive of the fact that for the majority of data points, $\tilde{s}_2 < 0 < \tilde{s}_1$. This condition is indeed met for 85.8% of the ensemble of the data of Cardesa *et al.* (2013) and 85.2% of the ensemble of the data presented in § 4.

4. Data

In order to observe the dependences discussed in § 2 and validate the bounds that we derive in § 3 we must choose a suitable test case flow with access to the full VGT. In order for our assumptions of incompressibility, homogeneity and isotropy to be largely fulfilled we require data from a region of fully developed turbulence, which in the Richardson–Kolmogorov phenomenology should exhibit statistical isotropy and homogeneity at the small scales (but in practice of course will only closely approximate this). George & Hussein (1991) illustrate that at finite Reynolds numbers there is no such thing as a perfectly isotropic flow and thus quantify the degree of (an)isotropy by using their parameters K_1, K_2, K_3 and K_4 . Taylor (1935) derives the value for all four of these parameters to be unity for homogeneous isotropic turbulence (HIT). Further, George & Hussein (1991) produce an exhaustive list of the values of these parameters in a wealth of different flow configurations and experiments (their tables 1 and 2). Departure from unity for these parameters can thus be used to assess

the degree of (an)isotropy of the small scales of a flow and this departure can easily be compared to that for other flows.

In the event of small-scale anisotropy (to whatever extent) the choice of source plane for the reduced VGT, i.e. which 2×2 block of the VGT, is no longer an arbitrary choice but must be carefully considered. This is further discussed in §7. Whilst many numerical studies with excellent HIT data exist this will not allow us to examine the effect of large-scale anisotropy on the choice of source plane for the reduced VGT. In order to do this we must instead consider a shear flow. We thus choose to use a mixing layer, which can be considered the most canonical of all the free shear flows. Winant & Browand (1974) state, ‘the region between two parallel streams moving at different speeds is the simplest free shear flow which can be considered’ and is thus the ideal flow against which to test our analyses.

The data that we choose are identical to those used by Buxton, Laizet & Ganapathisubramani (2011*b*) of a nominally two-dimensional, planar mixing layer produced by means of a direct numerical simulation (DNS) of two flows of different free-stream velocities (U_1 and U_2 , in the ratio $U_1/U_2 = 2$) either side of a splitter plate of thickness h , similar to the study of Laizet, Lardeau & Lamballais (2010). The computational domain ($L_{x_1} \times L_{x_2} \times L_{x_3}$) = (230.4*h* × 48*h* × 28.8*h*) is discretised on a Cartesian mesh that is stretched in the cross-stream (x_2) direction of (2049 × 513 × 256) mesh nodes. The stretching of the mesh in the cross-stream direction leads to a minimal mesh size of $\Delta x_2 \approx 0.03h$. The time step, $\Delta t = 0.05h/U_c$, where $U_c = (U_1 + U_2)/2$ is the mean convection velocity, is low enough to satisfy the Courant–Friedrichs–Lewy condition, ensuring temporal stability of the solution.

A sub-domain that consisted of the final 301 (× 513 × 256) mesh nodes in the streamwise (x_1) direction was isolated and three time steps that were sufficiently well spaced in time to ensure statistical independence were saved. This sub-domain is in the far field of the mixing layer in which the turbulence is fully developed with self-similar mean velocity profiles throughout, with all subsequent data and analysis presented in this manuscript coming from this sub-domain. The Reynolds number based on U_c and h (Re_W) is 1000 and the Reynolds number based on the Taylor microscale, computed assuming isotropic turbulence (Taylor 1935), is $Re_\lambda \approx 270$ along the centreline.

The code ‘incompact3d’ (Laizet & Lamballais 2009), based on sixth-order compact schemes for spatial discretisation and second-order Adams–Bashforth schemes for time advancement, is used to solve the incompressible non-dimensionalised Navier–Stokes equations. To treat the incompressibility condition a projection method is used requiring the solution of a Poisson equation for the pressure. This equation is fully solved in spectral space via the use of the relevant three-dimensional fast Fourier transforms (FFT). The boundary conditions are inflow/outflow in the streamwise direction (velocity boundary conditions of the Dirichlet type), free slip in the cross-stream direction at $x_2 = \pm L_{x_2}/2$ and periodic in the spanwise direction at $x_3 = \pm L_{x_3}/2$. The pressure mesh is staggered from the velocity mesh to avoid spurious pressure oscillations. Using the concept of modified wavenumber, the divergence-free condition is ensured up to the machine accuracy. More details on the simulation, including the generation of the inlet/initial conditions (including the boundary layers on both sides of the splitter plate), can be found in Laizet *et al.* (2010) and more details about the code, its validation and the original treatment of the pressure in spectral space can be found in Laizet & Lamballais (2009).

In order to ensure that only data in the turbulent region of the flow are considered a criterion based on the enstrophy was devised. Thresholds based on enstrophy have

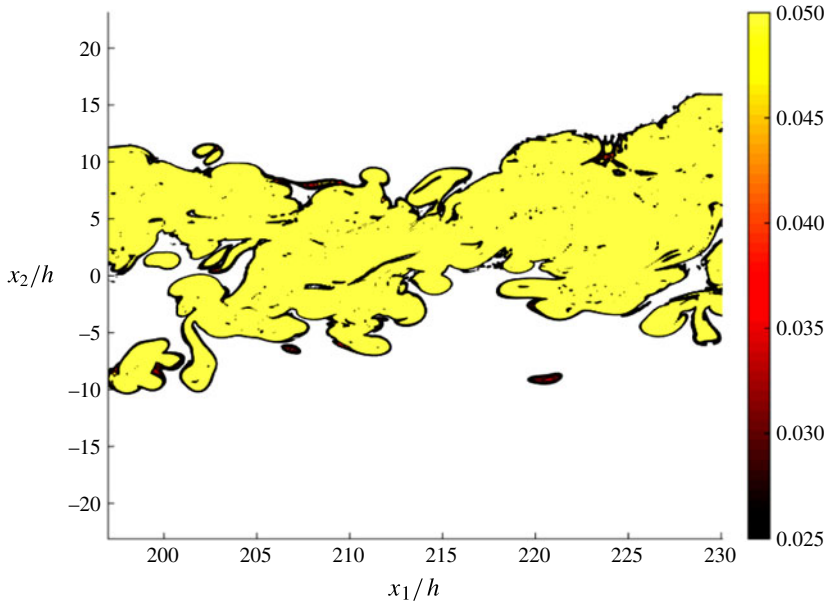


FIGURE 3. (Colour online) Instantaneous contours of enstrophy for a plane of constant x_3 .

been found to be the most suitable for the identification of turbulent/non-turbulent fluid in free shear flows (Bisset *et al.* 2002). Thus a threshold based on the mean enstrophy for each time step, $\omega_{inres.}^2 = 0.025\langle\omega^2\rangle$, was chosen based on figure 3 to ensure that data from the potential flow region were discarded. Data points with enstrophies below 2.5% of the means were removed, accounting for some 30% of the original data.

4.1. Isotropy validation

The assumption of local isotropy requires that there is no statistically preferential direction at a given point within the flow. Consequently the mean square of each of the off-diagonal terms of the VGT ought to be equal to each other and equal to twice the mean square of each of the diagonal terms (George & Hussein 1991). A sixth-order Lagrange interpolating polynomial numerical scheme was used to compute the velocity gradients. For grid flow, values of the isotropic parameters of George & Hussein (1991) $K_1 \in [1.04, 1.09]$ and $K_3 \in [0.72, 0.8]$ are deemed reasonable approximations of isotropy (Valente & Vassilicos 2014). Thus it can be seen that the turbulence in the far field of the mixing layer can be reasonably approximated as being locally isotropic (better in fact than these recent grid flows):

$$K_1 = 2 \left\langle \left(\frac{\partial u_1}{\partial x_1} \right)^2 \right\rangle / \left\langle \left(\frac{\partial u_2}{\partial x_1} \right)^2 \right\rangle = 1.0582, \quad (4.1)$$

$$K_2 = 2 \left\langle \left(\frac{\partial u_1}{\partial x_1} \right)^2 \right\rangle / \left\langle \left(\frac{\partial u_3}{\partial x_1} \right)^2 \right\rangle = 1.0406, \quad (4.2)$$

$$K_3 = 2 \left\langle \left(\frac{\partial u_1}{\partial x_1} \right)^2 \right\rangle / \left\langle \left(\frac{\partial u_1}{\partial x_2} \right)^2 \right\rangle = 0.8742, \quad (4.3)$$

Local isotropy condition	\tilde{A}_{ij} estimate	Percentage difference (%)
$\frac{\langle pq \rangle}{\langle p^3 \rangle} = \frac{7}{6}$	1.1384	-2.42
$\frac{\langle pq \rangle}{\langle \omega_i S_{ij} \omega_j \rangle} = -\frac{1}{15}$	-0.0705	5.75

TABLE 1. Comparison of statistical results of the reduced VGT invariants with those derived using the assumption of homogeneous isotropic turbulence in (2.1) and (2.2).

$$K_4 = 2 \left\langle \left(\frac{\partial u_1}{\partial x_1} \right)^2 \right\rangle / \left\langle \left(\frac{\partial u_1}{\partial x_3} \right)^2 \right\rangle = 0.9166. \tag{4.4}$$

Under the assumption of local isotropy, the dissipation rate can be expressed as

$$\epsilon = \begin{cases} 15\nu \left\langle \frac{\partial u_i}{\partial x_j} \right\rangle & \text{if } i = j, \\ 7.5\nu \left\langle \frac{\partial u_i}{\partial x_j} \right\rangle & \text{if } i \neq j. \end{cases} \tag{4.5}$$

For the current data the approximations ranged from $0.897\langle\epsilon\rangle$ to $1.086\langle\epsilon\rangle$, where $\langle\epsilon\rangle$ is the mean rate of dissipation computed without assumption as $\langle\epsilon\rangle = 2\nu\langle S_{ij}S_{ij}\rangle$. The closest dissipation estimate assuming local isotropy was obtained using the $\partial u_2/\partial x_2$ component, giving a value of $1.011\langle\epsilon\rangle$. Conventionally, the first diagonal term is used which gives an estimate of $0.949\langle\epsilon\rangle$.

Cardesa *et al.* (2013) derived the relationships in (2.1) and (2.2), relating the invariants of the reduced VGT to the mean enstrophy amplification rate $\langle\omega_i S_{ij} \omega_j\rangle$ using the assumptions of homogeneity and local isotropy. A further consideration of the validity of the assumption of local isotropy for the mixing layer data, in the context of the reduced VGT, is presented in table 1. It can thus be seen that the flow is, again, on the whole close to meeting the conditions for local isotropy.

5. Validation of our bounds against the mixing layer data

5.1. Invariants of the reduced VGT

Figure 4 shows the joint p.d.f. between p and q which again shows the characteristic ‘teapot’ shape reported in Cardesa *et al.* (2013) and Fiscaletti *et al.* (2014) for a variety of turbulent flows. These new data add further credence to the notion that the shape of the p - q joint p.d.f. is also a ‘universal’ feature of turbulent flows, similarly to that for the full invariants Q and R (Elsinga & Marusic 2010).

The joint p.d.f.s between the invariants of the VGT and those for the reduced VGT are presented in figure 5 which shows the joint p.d.f.s between Q and $(-p^2 + q)$ (a) and R and $-pq$ (b). There is a clear trend for Q to be distributed along the line $Q = (-p^2 + q)$, derived in (2.3), in figure 5(a), with a stretching of the contours of the joint p.d.f. along this line meaning localised peaks (modes) in the conditional p.d.f.s of Q against $(-p^2 + q)$. The contours are also observed to be stretched along $(-p^2 + q) = 0$, but this is subsequently shown to be a generic property of a trace-free 3×3 matrix. It can be seen that there is a much greater spread of the data for $Q > (-p^2 + q)$

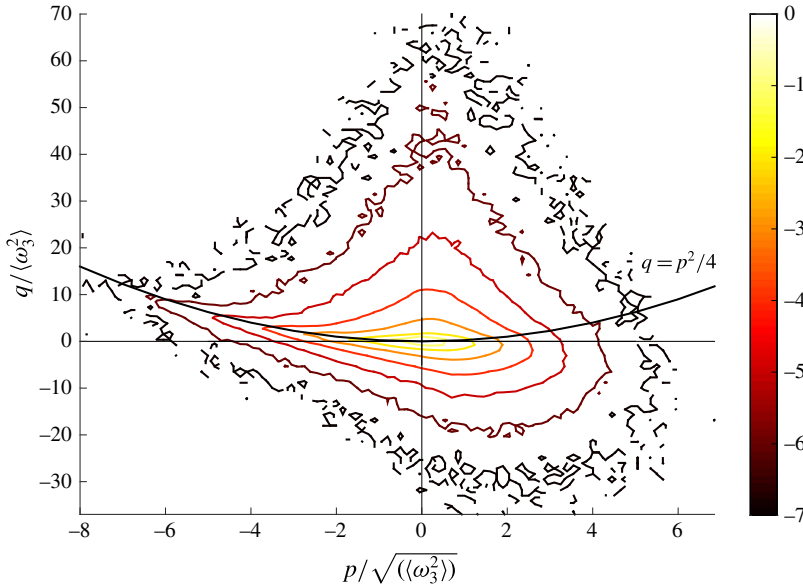


FIGURE 4. (Colour online) Joint p.d.f. of reduced VGT invariants p and q . Contours scale logarithmically.

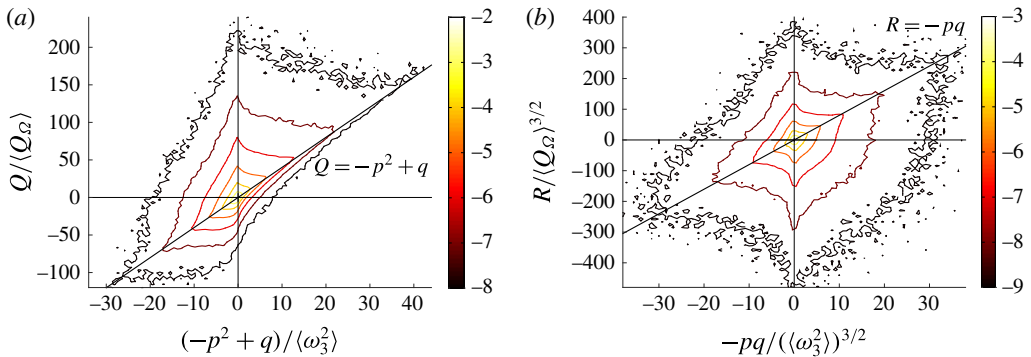


FIGURE 5. (Colour online) Joint p.d.f.s of Q (a) and R (b) against their constituent terms from the reduced VGT. Contours scale logarithmically.

than for $Q < (-p^2 + q)$ indicating that as the excess of rotation (swirling) over strain rate for the fluid element becomes greater, then less information regarding the VGT is carried in the invariants of the reduced VGT. Figure 5(b) on the other hand shows very little structure whatsoever to the contour levels of the joint p.d.f. between R and $-pq$, derived in (2.4). This emphasises the difficulty in gleaning information on the third invariant R , which is a property of three-dimensional turbulence that is not present in two-dimensional turbulence, from the reduced VGT, which is of course a two-dimensional projection of the full VGT.

The dependence of Q on the individual invariants, p (a) and q (b), of the reduced VGT is illustrated in figure 6 with $Q = -p^2$ and $Q = q$ shown as the dashed lines respectively. The first reduced invariant, p , is an indication of the compressibility of the flow when projected onto a 2D plane. Buxton, Laizet & Ganapathisubramani

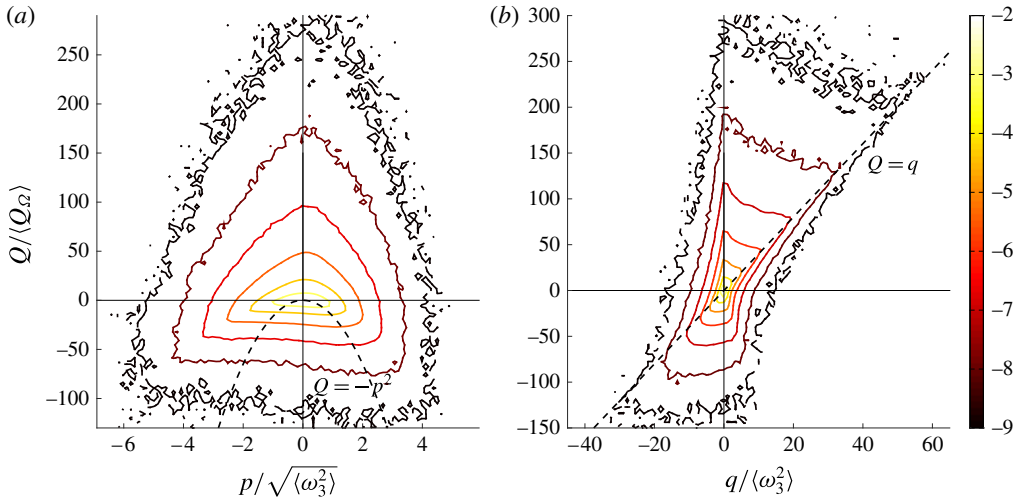


FIGURE 6. (Colour online) Joint p.d.f.s of Q against the invariants of the reduced VGT p (a) and q (b). Contours scale logarithmically.

(2011a) show that artificial compressibility introduced by experimental noise increases and indeed alters the distribution of the Q – R joint p.d.f. No distribution around $Q = -p^2$ whatsoever is observed for the estimation of Q from the ‘compressibility’ invariant, p in the joint p.d.f. of figure 6(a). In contrast it can be seen from the joint p.d.f. in figure 6(b) that the distribution of the contours about $Q = q$ is similar to that for $Q = -p^2 + q$ in figure 5(a) with strong peaks in probability observed for $Q = q$. It is observed that the sign of q is an excellent predictor of the sign of Q for $Q < 0$ (local excess of strain rate over rotation): 85.3% of the data for which $q < 0$ exhibits concurrent $Q < 0$ (the bottom left-hand quadrant of figure 6b). However, q being positive is a significantly inferior predictor of the sign of Q , with only 54.1% of data having a positive value of Q (local excess of rotation over strain rate) for $q > 0$. By inspection of the joint p.d.f. contours it can also be seen that the variance of the distribution of the joint p.d.f. when $Q > 0$ and $q > 0$ is significantly greater than that for when $Q < 0$ and $q < 0$, further reducing the quality of predictions for Q from q . It is thus argued that the two-dimensional projection of local straining is a far more accurate guide to the underlying three-dimensional physics than the projection of rotation.

In order to show that the strong dependence between Q and q is a property of Navier–Stokes turbulence and not a generic property of trace-free 3×3 matrices a synthetic divergence-free velocity field was produced for comparison. A $100 \times 100 \times 100$ domain of velocities modelled as Gaussian distributed uncorrelated noise with the same extrema as the velocity components of the DNS data was generated. Incompressibility was enforced by assigning u_1 , u_2 and $A_{33} = -(A_{11} + A_{22})$ and thereby computing u_3 . The resulting joint p.d.f.s of Q against p and q (equivalent to those in figure 6) are presented in figure 7. It can be seen that the shapes and peaks of the joint p.d.f.s in figure 6 are distinct from those of figure 7, particularly that of the joint p.d.f. between q and Q , and can therefore be assumed to result from the turbulent flow being examined and thus the Navier–Stokes equations. The observed stretching of the joint p.d.f. contours along $q = 0$ in figure 6(b) is additionally observed in

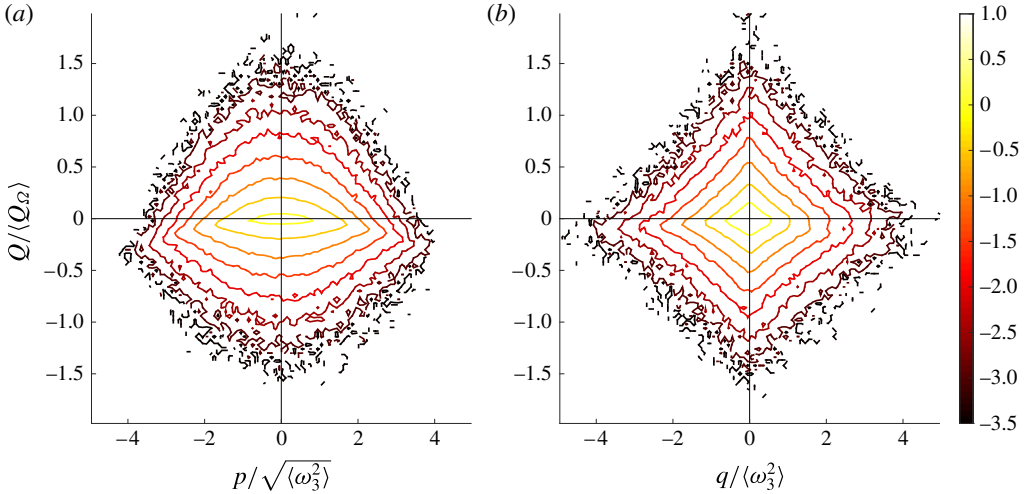


FIGURE 7. (Colour online) Joint p.d.f.s of Q against p (a) and q (b) for a synthetic velocity field of Gaussian noise. Contours scale logarithmically.

figure 7(b), showing that this is a property of a trace-free 3×3 matrix as opposed to representing the underlying physics of the Navier–Stokes equations.

5.2. The reduced strain-rate tensor

Figures 8 and 9 show joint p.d.f.s of the reduced and full strain-rate eigenvalues for the mixing layer data. Note that the interlacing bounds of (3.3) all hold and are sharp in the sense that the joint densities are non-zero arbitrarily close to each bound. The bounds derived in (3.7) are also observed to hold and are also sharp. The fact that these bounds are derived merely from incompressibility and are not representative of any physics themselves is illustrated in figure 10. This shows a similar series of joint p.d.f.s between s_i and \tilde{s}_2 formed from the synthetic, divergence-free, velocity field consisting of Gaussian distributed noise. The physics of Navier–Stokes turbulence are encapsulated in the statistical distributions of the joint p.d.f.s of figures 8 and 9 within these bounds.

It can be seen from figure 8 that the joint p.d.f.s are more skewed towards the bound given by $s_1 = -2\tilde{s}_1$ than that given by $s_1 = \tilde{s}_1$, and towards $s_3 = -\tilde{s}_1/2$ rather than $s_3 = \tilde{s}_1$. Similarly, figure 9 shows that the joint densities for \tilde{s}_2 are skewed towards $s_1 = -\tilde{s}_2/2$ as opposed to $s_1 = \tilde{s}_2$, and towards $s_3 = -2\tilde{s}_2$ rather than $s_3 = \tilde{s}_2$.

The modal values of the intermediate eigenvalue are seen to approximately follow $s_2 = \tilde{s}_1/4$ and $s_2 = -\tilde{s}_2/3$. The exact equations for the modal values of the full eigenvalues for each of the given reduced eigenvalues are

$$s_1 = -2.38\tilde{s}_1 + 2.54\langle\tilde{s}_1\rangle, \quad s_1 = -0.72\tilde{s}_2 - 0.79\langle\tilde{s}_2\rangle, \quad (5.1a,b)$$

$$s_2 = 0.22\tilde{s}_1 + 1.31\langle\tilde{s}_1\rangle, \quad s_2 = -0.33\tilde{s}_2 - 0.23\langle\tilde{s}_2\rangle, \quad (5.2a,b)$$

$$s_3 = -1.25\tilde{s}_1 - 1.53\langle\tilde{s}_1\rangle, \quad s_3 = -2.32\tilde{s}_2 + 3.43\langle\tilde{s}_2\rangle. \quad (5.3a,b)$$

Figure 11 shows the first three standardised moments of the full eigenvalues s_i , conditioned upon the respective reduced eigenvalues \tilde{s}_1, \tilde{s}_2 . The nomenclature $M(s_i|\tilde{s}_i)$

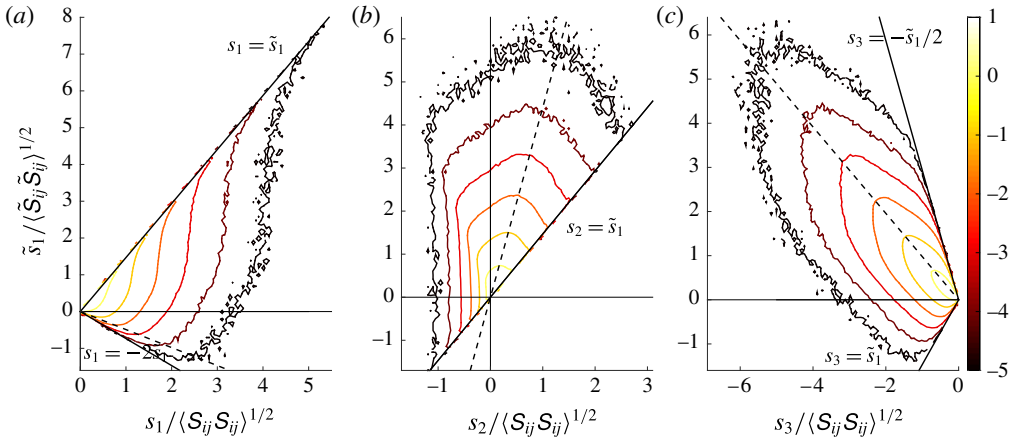


FIGURE 8. (Colour online) The joint p.d.f.s of \tilde{s}_1 against s_1 , s_2 and s_3 , (a)–(c) respectively. Contours scale logarithmically.

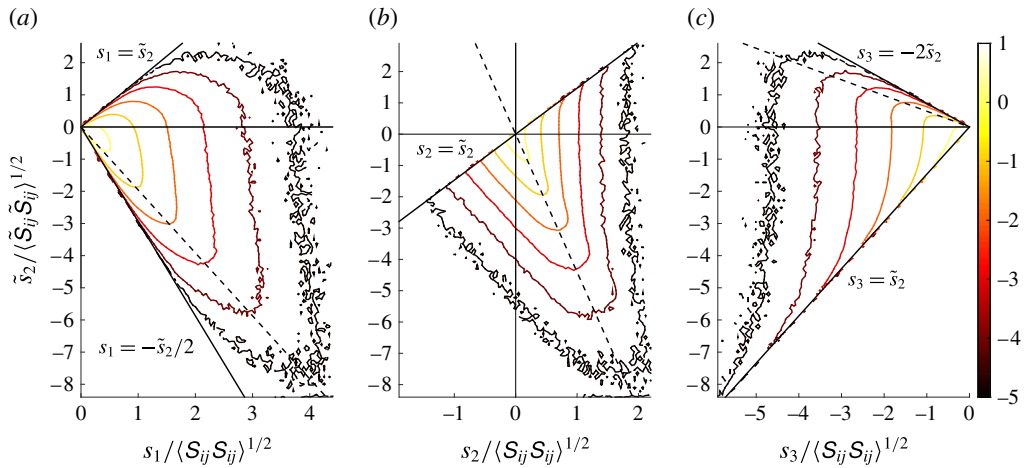


FIGURE 9. (Colour online) The joint p.d.f.s of \tilde{s}_2 against s_1 , s_2 and s_3 , (a)–(c) respectively. Contours scale logarithmically.

denotes the statistical moment of s_i given \tilde{s}_i , where M is either μ (mean, $\langle s_i \rangle$), σ^2 (variance, $\langle s_i^2 \rangle - \langle s_i \rangle^2$) or γ (skewness, $\langle s_i^3 \rangle / \langle s_i^2 \rangle^{3/2}$).

For the most commonly occurring case of $\tilde{s}_1 > 0$ and $\tilde{s}_2 < 0$ it can be seen that $\mu(s_2|\tilde{s}_i) > 0$. For $0 < \tilde{s}_1 / \langle \tilde{S}_{ij} \tilde{S}_{ij} \rangle^{1/2} < 1$ and $-1 < \tilde{s}_2 / \langle \tilde{S}_{ij} \tilde{S}_{ij} \rangle^{1/2} < 0$ it is observed that the ratio $\mu(s_3|\tilde{s}_i) : \mu(s_2|\tilde{s}_i) : \mu(s_1|\tilde{s}_i)$ is approximately $-4.8:1:3.8$, which is slightly higher than the reported modal ratios of roughly $-4:1:3$ (Ashurst *et al.* 1987; Tsinober *et al.* 1992) in other turbulent flows (for completeness the modal ratio for the entirety of the turbulent region of the mixing layer data is $-3.6:1:2.6$). Whilst the ratio $\mu(s_3|\tilde{s}_i) : \mu(s_2|\tilde{s}_i) : \mu(s_1|\tilde{s}_i)$ is observed to remain largely constant as \tilde{s}_1 is increased it is observed to decrease to approximately $-3.5:1:2.5$ for large magnitudes of (negative) \tilde{s}_2 . This is indicative of a relatively stronger extensive intermediate strain rate and hence more aggressive ‘sheet-forming’ topological evolution when \tilde{s}_2 is a higher magnitude negative value. Thus knowledge of the reduced strain-rate tensor

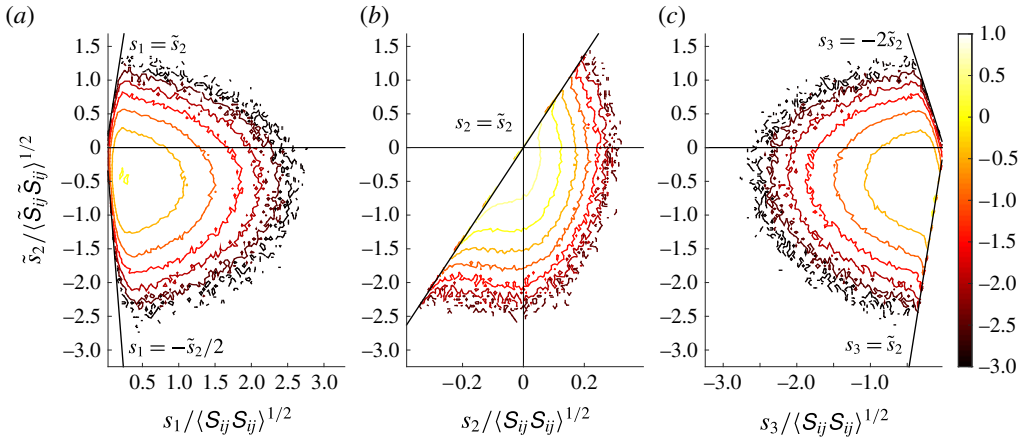


FIGURE 10. (Colour online) Joint p.d.f.s of \tilde{s}_2 against s_1 , s_2 and s_3 , (a)–(c) respectively, for a synthetic velocity field consisting of Gaussian distributed noise. Contours scale logarithmically.

eigenvalues gives us an indication of the intensity of the topological evolution of the fluid element in three dimensions.

The conditional means $\mu(s_1|\tilde{s}_1)$ and $\mu(s_3|\tilde{s}_1)$ behave similarly to the bounds of (3.6), in that their gradients change by a factor of around $-1/2$ as \tilde{s}_1 passes zero. The reduction in gradient of $\mu(s_2|\tilde{s}_1)$ as \tilde{s}_1 passes zero does not appear to be related to the bounds considered in the previous section. The means of the full eigenvalues s_1 and s_3 conditioned upon \tilde{s}_2 , shown in figure 11(b), behave similarly. However, when conditioned upon \tilde{s}_2 it is observed that the gradient of $\mu(s_2|\tilde{s}_2)$ not only changes its magnitude as it passes $\tilde{s}_2 = 0$ but also its sign, meaning that $\langle s_2 \rangle$ remains positive for all \tilde{s}_2 and hence ‘sheet-forming’ is favoured over ‘tube-forming’. Thus $\mu(s_2|\tilde{s}_1)$ more closely follows $\mu(s_3|\tilde{s}_1)$, whereas $\mu(s_2|\tilde{s}_2)$ varies as $\mu(s_1|\tilde{s}_2)$, resulting in preferential ‘tube-forming’ topological evolution when $\tilde{s}_1 < 0$, in agreement with Cardesa *et al.* (2013).

Such dependence upon the sign of the reduced eigenvalues is also prominent in the case of skewness. In particular, $\gamma(s_2|\tilde{s}_1)$ abruptly changes from positive to negative as \tilde{s}_1 passes zero. An explanation for this behaviour is suggested by the structure of the joint p.d.f. presented in figure 8(b). In particular, for $\tilde{s}_1 < 0$ the conditional density of s_2 is monotonic until the upper bound $s_2 = \tilde{s}_1$. However, for $\tilde{s}_1 > 0$, the conditional density has a maximum value strictly before the upper bound is met. Again, this behaviour is not indicated by the eigenvalue bounds of (3.6). Opposite behaviour to this is observed for $\gamma(s_3|\tilde{s}_1)$ with a decrease (and negative skewness) observed up until $\tilde{s}_1/\langle S_{ij}S_{ij} \rangle^{1/2} \approx 1$ before subsequently increasing as the unimodal behaviour of the joint p.d.f. of figure 8(c) becomes more significant. The skewness for all of the turbulent strain rates is subsequently observed to be uniform for large values of \tilde{s}_1 .

A similar change in $\gamma(s_3|\tilde{s}_2)$ can be observed in figure 11(f). Again, it can be seen from figure 9(c) that the conditional density changes from monotonic to unimodal as \tilde{s}_2 changes sign. This time, however, the change can be attributed to the bound $s_3 \leq \min\{\tilde{s}_2, -(\tilde{s}_1 + \tilde{s}_2)\}$. In particular, the second bound $s_3 \leq -(\tilde{s}_1 + \tilde{s}_2)$ is active when $2\tilde{s}_2 + \tilde{s}_1 \geq 0$, and this is most likely to be the case when \tilde{s}_2 is positive. Hence, in this range, the behaviour of s_3 is influenced by both reduced eigenvalues, serving to push the peak of the conditional p.d.f. away from the conservative bound $s_3 \leq -2\tilde{s}_2$

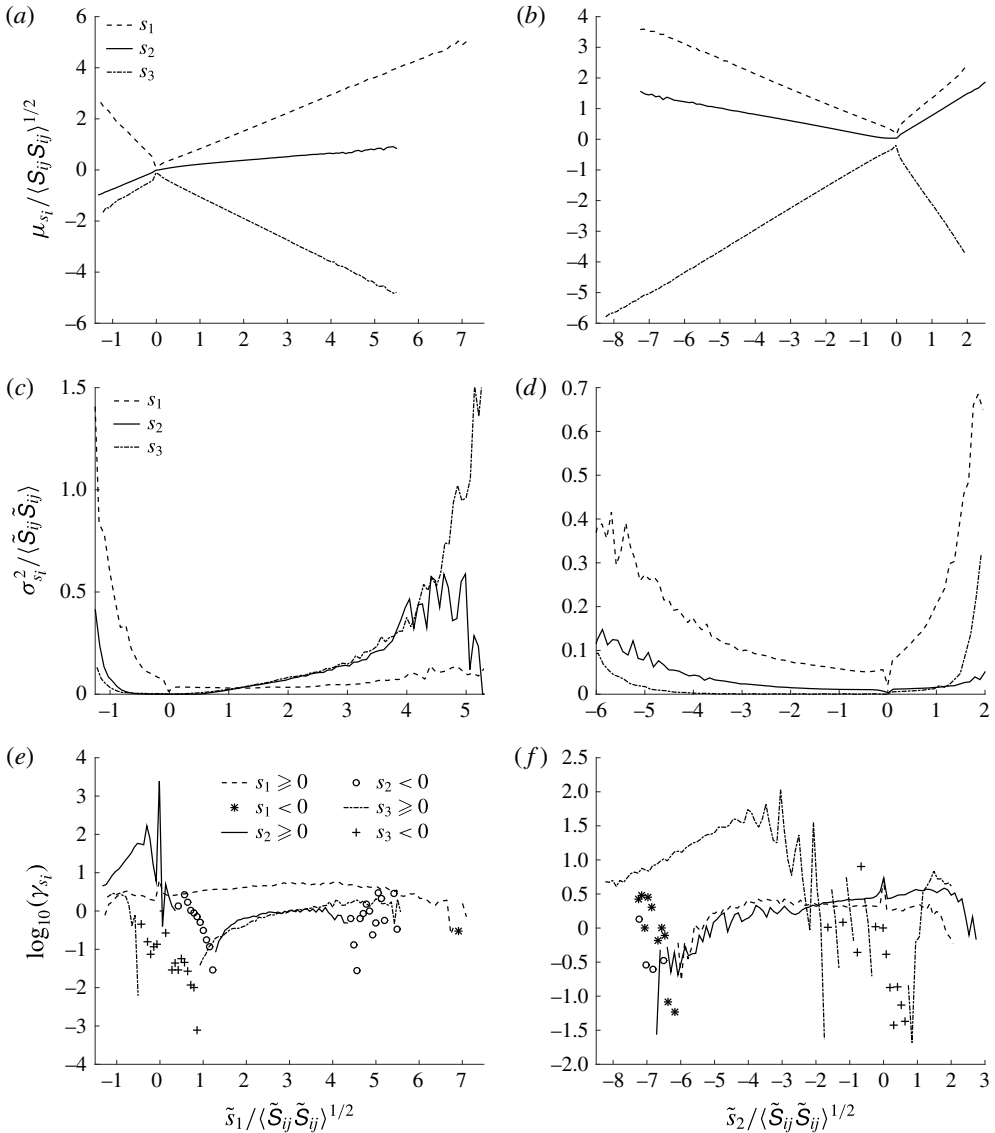


FIGURE 11. Statistical moments of the strain-rate eigenvalues conditioned on \tilde{s}_i . (a) Mean $\mu(s_i|\tilde{s}_1)$, (b) $\mu(s_i|\tilde{s}_2)$, (c) variance $\sigma^2(s_i|\tilde{s}_1)$, (d) $\sigma^2(s_i|\tilde{s}_2)$ (e) skewness $\gamma(s_i|\tilde{s}_1)$ and (f) $\gamma(s_i|\tilde{s}_2)$.

indicated in figure 9. It is observed that $\gamma(s_1|\tilde{s}_2)$ and $\gamma(s_2|\tilde{s}_2)$ follow a contrasting pattern to that for $\gamma(s_3|\tilde{s}_1)$, with constant skewness seen for lower magnitudes of \tilde{s}_2 and negative skewness seen at larger (negative) magnitudes.

The conditional variances represent the quality of information that each of the reduced eigenvalues \tilde{s}_1, \tilde{s}_2 contains about the full eigenvalues s_i . For example, figure 11(c) shows asymmetry of $\sigma^2(s_1|\tilde{s}_1)$, with higher conditional variance for $\tilde{s}_1 < 0$. Again, this is explained by the nature of the bound of (3.6): in the range $\tilde{s}_1 < 0$ the active bound on s_1 from (3.6) is $s_1 \geq -(\tilde{s}_1 + \tilde{s}_2)$; while in the range $\tilde{s}_1 > 0$ the bound $s_1 \geq \tilde{s}_1$ is most likely active. Hence, it is not unexpected that for

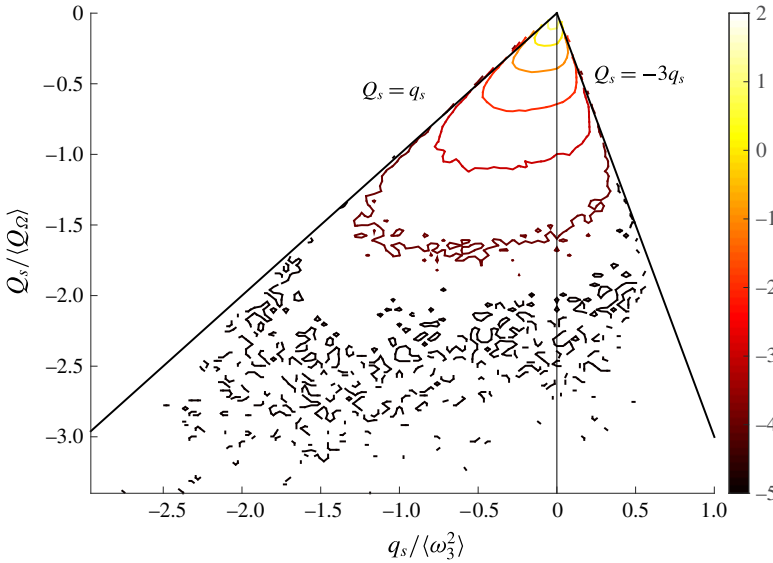


FIGURE 12. (Colour online) Joint p.d.f. of Q_S against q_S . Contours scale logarithmically.

a given $\alpha > 0$, we have $\sigma^2(s_1|\tilde{s}_1 = -\alpha) > \sigma^2(s_1|\tilde{s}_1 = \alpha)$. The variances for all s_i are observed to drop dramatically at $\tilde{s}_i = 0$ (although this is accentuated for s_1 due to the ‘peakiness’ of the distributions). This can be explained by the fact that for $\tilde{s}_i = 0$ the bounds observed in figures 8 and 9 force the modal values of the p.d.f.s of s_i to be located at zero, with monotonic, logarithmically decreasing tails, whereas the modal value moves away from the origin for all other \tilde{s}_i , thereby increasing the variance.

Figure 12 shows the joint p.d.f. between Q_S and q_S . The asymmetric sector bounds derived in (3.14), dependent upon the sign of q_S , are again observed to be sharp. It can be seen that the distribution is slightly skewed towards the bound of $Q_S \leq q_S$ for $q_S \leq 0$.

We show in (3.20) and (3.21) that the bounds on the mean values of the reduced strain-rate eigenvalues, $\langle \tilde{s}_i \rangle$, are a function of the kurtosis of A_{11} (κ). Further, figure 2, illustrates that κ is itself a function of the cross-stream direction x_2 . Incorporating the entire turbulent region of the mixing layer as defined by the region in which the enstrophy exceeded the enstrophy threshold (see § 4) the mean kurtosis is computed to be $\kappa = 9.4$ leading to the bounds

$$0.40 \leq \frac{\langle \tilde{s}_1 \rangle}{\sqrt{\frac{3}{2} \left\langle \left(\frac{\partial u_1}{\partial x_1} \right)^2 \right\rangle^{1/2}}} \leq 1, \quad -1 \leq \frac{\langle \tilde{s}_2 \rangle}{\sqrt{\frac{3}{2} \left\langle \left(\frac{\partial u_1}{\partial x_1} \right)^2 \right\rangle^{1/2}}} \leq -0.40, \quad (5.4a,b)$$

which are indicated by vertical lines on the inset of figure 13 showing the p.d.f.s of \tilde{s}_i . Equations (3.20) and (3.21) and figure 2, however, illustrate that tighter bounds on $\langle \tilde{s}_i \rangle$ can be found closer to the centreline of the mixing layer than the periphery. The appropriately normalised expected values are 0.58 and -0.66 , respectively, which can be seen to lie within the expected ranges. We observe, however, that $-\langle \tilde{s}_1 \rangle / \langle \tilde{s}_2 \rangle = 0.88$ instead of taking the value 1, which would be the case if the flow were truly isotropic.

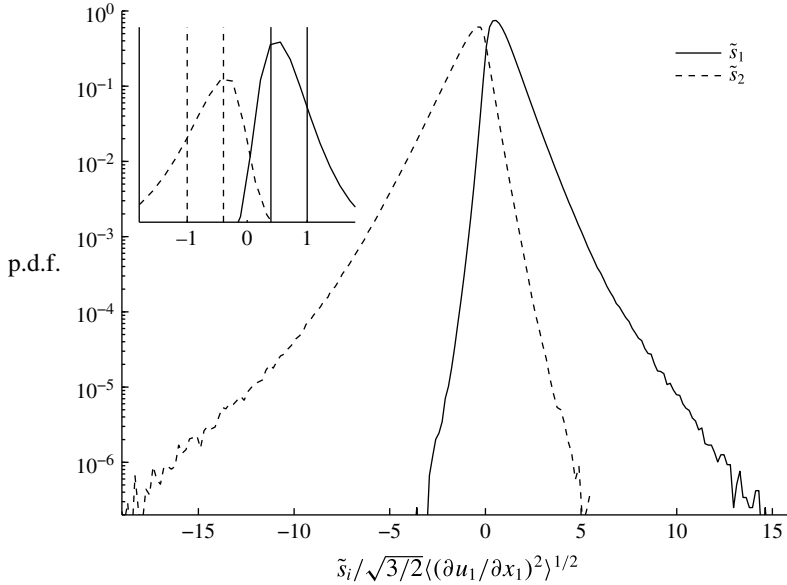


FIGURE 13. P.d.f. of the reduced strain-rate tensor eigenvalues. The inset shows the bounds on $\langle \tilde{s}_i \rangle$ derived in (3.20) and (3.21).

Further, assuming that (3.27) holds and using $\kappa = 9.4$, the upper bounds of $\sigma_{\tilde{s}_{1,2}}^2$ from (3.26) are 1.26 and 1.76, respectively. These compare to their respective numerical values of 0.980 and 1.388. We note that the conjecture $\langle p_S \sqrt{X} \rangle > 0$ is supported by the distributions of the reduced eigenvalues shown in figure 13, where it can be seen that \tilde{s}_2 takes a wider range of values than \tilde{s}_1 . This supports the observation of Cardesa *et al.* (2013) that the tails of the p.d.f. of \tilde{s}_2 are more extensive than those of \tilde{s}_1 .

Equation (3.3) shows that knowledge of the magnitude of the reduced strain-rate eigenvalues allows us to place bounds on s_i . By making use of the properties of the expectation operator we may additionally write

$$\langle s_3 \rangle \leq \langle \tilde{s}_2 \rangle \leq \langle s_2 \rangle \leq \langle \tilde{s}_1 \rangle \leq \langle s_1 \rangle \tag{5.5}$$

and thus we can see that we may bound the mean values of the strain-rate eigenvalues themselves from (3.20) and (3.21). Figure 13 shows that these bounds are actually reasonably tight for a typical free shear flow. Furthermore, knowledge of higher-order moments of \tilde{s}_1 and \tilde{s}_2 (such as $\sigma_{\tilde{s}_{1,2}}^2$), will give us a better indication of the strength of these bounds that we may place on s_i .

6. Eigenvectors of S_{ij} and \tilde{S}_{ij}

Further to the discussion presented in § 1, (1.4) shows that the interaction between strain rate and rotation, and the enstrophy amplification term $\omega_i S_{ij} \omega_j$ is strongly dependent upon the alignment cosines between the vorticity vector and the strain-rate eigenvectors. The mean value of the enstrophy amplification term can be shown to relate to the skewness of one of the components of the VGT under the assumption of local isotropy (Betchov 1956):

$$\langle \omega_i S_{ij} \omega_j \rangle = -\frac{7}{6\sqrt{15}} \langle \omega^2 \rangle^{3/2} \gamma_0, \tag{6.1}$$

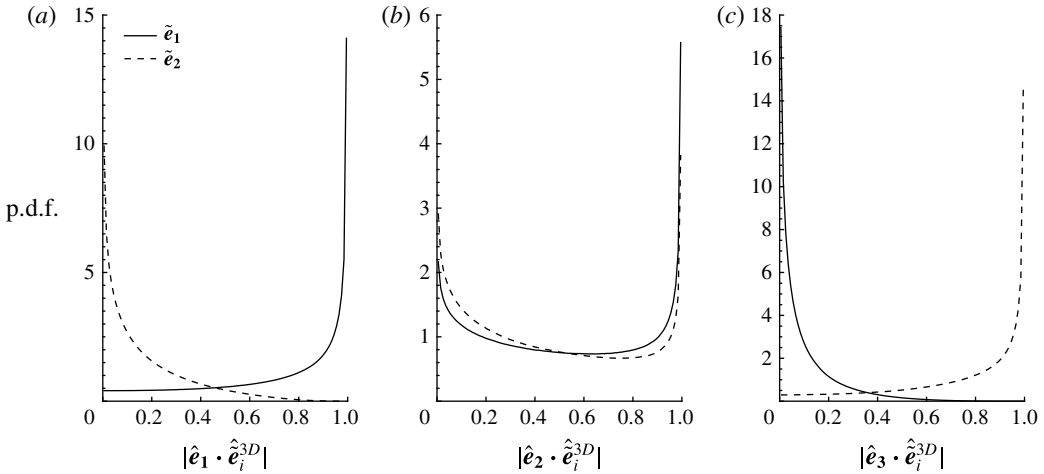


FIGURE 14. P.d.f.s of the alignment cosines between the three-dimensional embedding of the eigenvectors of \tilde{S}_{ij} and the eigenvectors of S_{ij} .

$$\gamma_0 = \frac{\left\langle \left(\frac{\partial u_1}{\partial x_1} \right)^3 \right\rangle}{\left\langle \left(\frac{\partial u_1}{\partial x_1} \right)^2 \right\rangle^{3/2}}, \quad (6.2)$$

and γ_0 can be directly measured without recourse to 3D3C data. Cardesa *et al.* (2013) extended this to consideration of the reduced VGT invariants and showed, via (2.1) and (2.2) that

$$\langle \omega_i S_{ij} \omega_j \rangle = -15 \langle pq \rangle = -\frac{105}{6} \langle p^3 \rangle. \quad (6.3)$$

However, this does not reveal anything of the directionality of the two-dimensional projection of the three strain-rate eigenvectors instantaneously, or indeed whether this is reflected in the eigenvectors (eigenframe) of the reduced strain-rate tensor. These are defined in a similar convention to those of the full strain-rate tensor, with \tilde{e}_1 corresponding to the first reduced eigenvalue, \tilde{s}_1 , and \tilde{e}_2 corresponding to \tilde{s}_2 .

P.d.f.s of the alignment cosines between the three-dimensional embedding of \tilde{e}_i , defined as $\hat{e}_i^{3D} = [\tilde{e}_{ix_1}, \tilde{e}_{ix_2}, 0]^T$, and e_i are presented in figure 14. This three-dimensional embedding of the reduced strain-rate eigenvectors was used such that the out of plane component of e_i , e_{ix_3} , was included in the norm of e_i when computing the alignment cosines

$$|\cos \theta| = \left| \hat{e}_i^{3D} \cdot \hat{e}_i \right| \quad (6.4)$$

in which \hat{a} denotes a (normalised) unit vector. This is an important consideration for the case in which the eigenvectors of the strain-rate tensor are predominantly oriented perpendicularly to the source plane of the reduced VGT. In this case the alignment between the two-dimensional projection of e_i ($= [e_{ix_1}, e_{ix_2}]^T$) and \tilde{e}_i is heavily distorted by the artificially small norm of the two-dimensional projection of vector e_i .

Figure 14 shows that there is a very strong preferential alignment between e_1 and the three-dimensional embedding of \tilde{e}_1 . Whilst there is a progressively increasing probability of the cosine of the angle between the two vectors for increasing $|\cos \theta|$ there is an extremely sharp spike at $|\cos \theta| = 1$. Qualitatively similar behaviour is also observed for the alignment cosine between e_3 and the three-dimensional embedding

of \tilde{e}_2 , the most compressive of the reduced strain-rate eigenvectors. This evidences the fact that as long as the norm of e_i factors in the out of plane component (with respect to the reduced VGT source plane) then the eigenvectors of the reduced strain-rate tensor are an excellent predictor of the two-dimensional projection of the full, three-dimensional strain-rate eigenvectors. Evidently the two-dimensional projection of the strain-rate eigenvectors can be described by a vector sum of the unit eigenvectors of \tilde{S}_{ij} . This requires that in cases in which the two-dimensional projection of e_i is instantaneously aligned in parallel with \tilde{e}_1 it must be aligned perpendicularly to \tilde{e}_2 and so forth. This is also reflected in the figure with large modal peaks at $|\hat{e}_1 \cdot \hat{e}_2^{3D}| \approx 0$ and $|\hat{e}_3 \cdot \hat{e}_1^{3D}| \approx 0$. The loci of the alignment cosines between the two-dimensional projections of e_i and \tilde{e}_i are thus circles centred upon the origin with unity radius.

In contrast figure 14 also shows that the alignment between e_2 and the three-dimensional embedding of the reduced strain-rate eigenvectors is bimodal. There are peaks corresponding to parallel and perpendicular alignment with both \tilde{e}_1^{3D} and \tilde{e}_2^{3D} , although parallel alignment is more likely for both. It can therefore be seen that there is a minimum preferential alignment at approximately $|\hat{e}_2 \cdot \hat{e}_1^{3D}| = 0.64$, which corresponds to an angle $\theta_{\hat{e}_1, \hat{e}_2} \approx 0.9$ between the two vectors and a corresponding minimum preferential alignment at approximately $|\hat{e}_2 \cdot \hat{e}_2^{3D}| = 0.73$ corresponding to $\theta_{\hat{e}_1, \hat{e}_2} \approx 0.7$.

Whilst $\tilde{s}_2 \leq \tilde{s}_1$, by definition, both $\tilde{s}_1 \leq 0$ and $\tilde{s}_2 \geq 0$ are possible meaning that the ‘most extensive’ reduced eigenvalue can in fact be compressive and the ‘most compressive’ reduced eigenvalue can be extensive. Figure 15 shows the alignment cosines between e_i and the three-dimensional embedding of \tilde{e}_i , similar to figure 14, conditioned on the special cases of $\tilde{s}_1 < 0$ (*a-c*) and $\tilde{s}_2 > 0$ (*d-f*). Both of these special cases are shown to have higher-order statistical moments of greater magnitude for the strain-rate eigenvalues conditioned on \tilde{s}_i than for the more common occurrences of $\tilde{s}_1 > 0$ and $\tilde{s}_2 < 0$ in figure 11, in addition to larger gradients of these statistical moments with respect to \tilde{s}_i .

We observe the same trend for a dominant parallel alignment tendency between the most compressive reduced strain-rate eigenvector (\tilde{e}_2) and the compressive strain-rate eigenvector (e_3) in the case of two compressive reduced strain rates, $\tilde{s}_2 \leq \tilde{s}_1 < 0$ (figure 15c). Similarly, there is a preferential parallel alignment between the most extensive reduced strain-rate eigenvector (\tilde{e}_1) and the extensive strain-rate eigenvector in the case of two extensive reduced strain rates, $0 < \tilde{s}_2 \leq \tilde{s}_1$ (figure 15d). The alignment of the intermediate strain-rate eigenvector with \tilde{e}_i is now no longer bimodal. It can be seen that there is now a preferential alignment with the three-dimensional embedding of the most extensive reduced strain-rate eigenvector (\tilde{e}_1) for the case of two compressive reduced strain rates (figure 15b) and with the most compressive reduced strain-rate eigenvector (\tilde{e}_2) for the case of two extensive reduced strain rates (figure 15e). It is thus observed that the intermediate strain-rate eigenvector, whose corresponding eigenvalue magnitude is bounded by the extensive and compressive strain rates, preferentially aligns in parallel with the eigenvector of the lower magnitude reduced strain-rate eigenvalue in these special cases. The alignment tendencies of $|\hat{e}_1 \cdot \hat{e}_i^{3D}|$ in figure 15(a) and $|\hat{e}_3 \cdot \hat{e}_i^{3D}|$ in figure 15(f) shows that there is zero probability of parallel alignment between the three-dimensional embedding of the reduced strain-rate eigenvectors and the extensive strain-rate eigenvector for the case of two compressive reduced strain rates (figure 15a) and the compressive strain-rate eigenvector for the case of two extensive reduced strain rates (figure 15f).

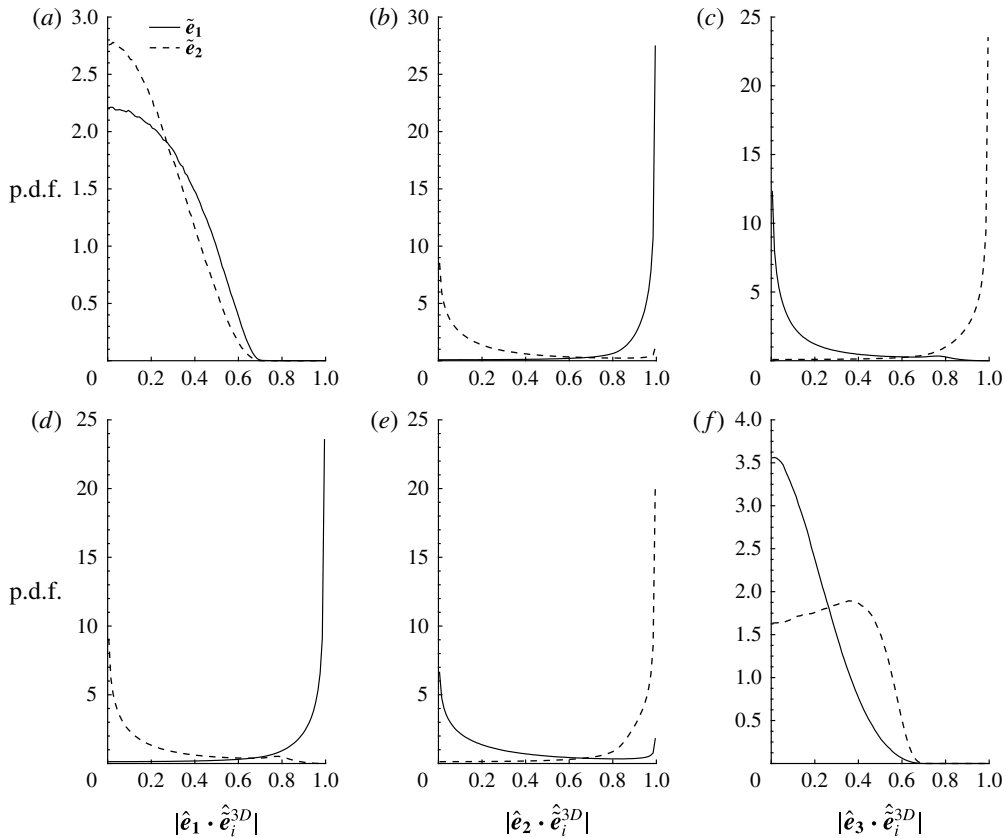


FIGURE 15. Conditional p.d.f.s of the alignment cosines between the three-dimensional embedding of the eigenvectors of \tilde{S}_{ij} and the strain-rate eigenvectors, similar to figure 14. (a–c) Conditioned on $\tilde{s}_1 < 0$, (d–f) conditioned on $\tilde{s}_2 > 0$.

This is indicative of the fact that for these special cases, for which Cardesa *et al.* (2013) were directly able to infer the sign of s_2 from the reduced VGT data, the corresponding strain-rate eigenvectors are oriented out of plane with respect to the source plane for the reduced VGT.

7. Reduced VGT interrogation plane

The assumption of local isotropy for turbulence is a restrictive one that is often only closely approximated by real turbulent flows (George & Hussein 1991), requiring statistical invariance to any direction within the flow. Indeed it can be seen in §4.1 that although the assumption is considered to be reasonable for the present data it is not fulfilled precisely. This led to the development of the less restrictive assumption of local axisymmetry (Batchelor 1946; Chandrasekhar 1950) in which there is a rotational symmetry about a given axis for the statistics of the VGT. (NB for both isotropic and axisymmetric turbulence the assumption of homogeneity, that is a statistical independence from location within the flow field, is additionally required.) The assumption of local axisymmetry is thus particularly relevant to flows that have an obvious preferential direction with regards to the VGT. In the present study the

Local axisymmetry condition	LHS/RHS
$\left\langle \left(\frac{\partial u_x}{\partial x_{r\theta_1}} \right)^2 \right\rangle = \left\langle \left(\frac{\partial u_x}{\partial x_{r\theta_2}} \right)^2 \right\rangle$	0.496
$\left\langle \left(\frac{\partial u_{r\theta_1}}{\partial x_x} \right)^2 \right\rangle = \left\langle \left(\frac{\partial u_{r\theta_2}}{\partial x_x} \right)^2 \right\rangle$	1.025
$\left\langle \left(\frac{\partial u_{r\theta_1}}{\partial x_{r\theta_1}} \right)^2 \right\rangle = \left\langle \left(\frac{\partial u_{r\theta_2}}{\partial x_{r\theta_2}} \right)^2 \right\rangle$	0.927
$\left\langle \left(\frac{\partial u_{r\theta_1}}{\partial x_{r\theta_2}} \right)^2 \right\rangle = \left\langle \left(\frac{\partial u_{r\theta_2}}{\partial x_{r\theta_1}} \right)^2 \right\rangle$	1.135
$\left\langle \left(\frac{\partial u_{r\theta_1}}{\partial x_{r\theta_1}} \right)^2 \right\rangle = \frac{1}{3} \left\langle \left(\frac{\partial u_x}{\partial x_x} \right)^2 \right\rangle + \frac{1}{3} \left\langle \left(\frac{\partial u_{r\theta_1}}{\partial x_{r\theta_2}} \right)^2 \right\rangle$	0.924
$\left\langle \left(\frac{\partial u_{r\theta_1}}{\partial x_{r\theta_2}} \right) \left(\frac{\partial u_{r\theta_2}}{\partial x_{r\theta_1}} \right) \right\rangle = \frac{1}{6} \left\langle \left(\frac{\partial u_x}{\partial x_x} \right)^2 \right\rangle - \frac{1}{3} \left\langle \left(\frac{\partial u_{r\theta_1}}{\partial x_{r\theta_2}} \right)^2 \right\rangle$	0.937
$\left\langle \left(\frac{\partial u_x}{\partial x_{r\theta_1}} \right) \left(\frac{\partial u_{r\theta_1}}{\partial x_x} \right) \right\rangle = \left\langle \left(\frac{\partial u_x}{\partial x_{r\theta_2}} \right) \left(\frac{\partial u_{r\theta_2}}{\partial x_x} \right) \right\rangle = -\frac{1}{2} \left\langle \left(\frac{\partial u_x}{\partial x_x} \right)^2 \right\rangle$	0.862/0.937

TABLE 2. Conditions on velocity gradients for locally axisymmetric turbulence (from George & Hussein 1991).

boundary conditions in the x_3 direction are periodic, and the growth rate of the mixing layer (and hence mean shear in the streamwise direction) is considered small in the far field, whereas there is a significant shear in the cross-stream (x_2) direction.

George & Hussein (1991) derived seven velocity gradient relations that are satisfied by locally axisymmetric turbulence, given in table 2, in which x_x is defined as the preferred flow direction which is assumed to be in the x_2 direction of the present mixing layer. The two axes that define the symmetry plane, assumed to be the x_1 - x_3 plane for the present mixing layer, are denoted $x_{r\theta_1}$ and $x_{r\theta_2}$. It can be seen that the data largely satisfy the conditions for axisymmetric turbulence with the exception of the first condition which compares the square of the VGT components of the u_2 velocity in the x_1 direction, in which the mixing layer is spreading, and the u_2 velocity in the x_3 direction in which the boundary conditions are periodic. Some of the discrepancies may also be due to the ‘incorrect’ choice of preferred direction, which is likely to have components in both the x_2 and x_1 directions.

Approximations for the dissipation rate under the assumption of local axisymmetry were derived by George & Hussein (1991), with values compared to those computed with no assumptions:

$$\begin{aligned}
 \epsilon &= \nu \left[\frac{5}{3} \left\langle \left(\frac{\partial u_x}{\partial x_x} \right)^2 \right\rangle + 2 \left\langle \left(\frac{\partial u_x}{\partial x_{r\theta_2}} \right)^2 \right\rangle + 2 \left\langle \left(\frac{\partial u_{r\theta_1}}{\partial x_x} \right)^2 \right\rangle + \frac{8}{3} \left\langle \left(\frac{\partial u_{r\theta_1}}{\partial x_{r\theta_2}} \right)^2 \right\rangle \right] \\
 &= 1.042(\epsilon) \\
 &= \nu \left[- \left\langle \left(\frac{\partial u_x}{\partial x_x} \right)^2 \right\rangle + 2 \left\langle \left(\frac{\partial u_x}{\partial x_{r\theta_1}} \right)^2 \right\rangle + 2 \left\langle \left(\frac{\partial u_{r\theta_1}}{\partial x_x} \right)^2 \right\rangle + 8 \left\langle \left(\frac{\partial u_{r\theta_1}}{\partial x_{r\theta_1}} \right)^2 \right\rangle \right] \\
 &= 0.968(\epsilon),
 \end{aligned} \tag{7.1}$$

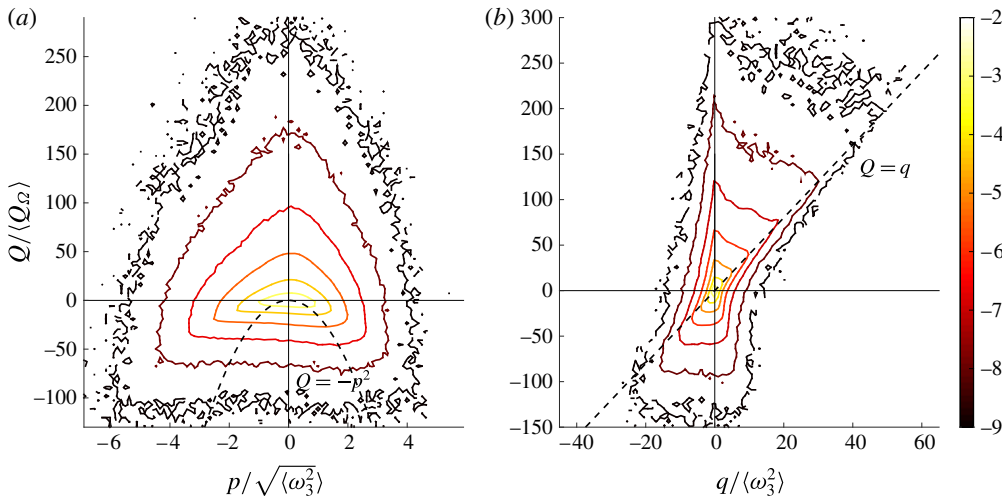


FIGURE 16. (Colour online) Joint p.d.f.s of full invariant Q against invariants p (a) and q (b) of the reduced VGT formed from data in the x_1 – x_3 plane. Contours scale logarithmically.

The range in dissipation estimates is lower than those computed under the assumption of local isotropy and the errors of 4.2% and –3.2% are small. The difference in the two values indicates that the flow is not truly locally axisymmetric; however, it can be seen that the two estimates are close to and encompass the true value.

For convenience Cardesa *et al.* (2013) chose the reduced VGT to consist of the upper left-hand quadrant of the VGT, encompassing all gradients in the streamwise and cross-stream directions. To some extent, however, this is an arbitrary choice as a reduced VGT can be formed from any plane within the flow for which data are available. *A priori* information on a flow field such as the planar mixing layer of this study would make it obvious that for an ‘infinite’ region of the flow (simulated here with periodic boundary conditions in the x_3 direction) the preferred plane to choose would indeed be the x_1 – x_2 plane. On the other hand if the flow is assumed to be well approximated by local axisymmetry, as is suggested by the results of (7.1), then the kinematics of the reduced VGT would not be expected to be identical if formed from the x_1 – x_3 plane (which is assumed to be the rotationally symmetric plane) as opposed to the x_1 – x_2 plane.

Figure 16 shows the joint p.d.f.s between Q and the invariants p (a) and q (b) of the reduced VGT formed from data in the x_1 – x_3 plane, similar to figure 6 which uses the reduced VGT formed in the x_1 – x_2 plane. It can be seen that both sets of figures look virtually identical. Furthermore the prediction of the sign of Q from the sign of q is also extremely similar to the data produced from the x_1 – x_2 plane with negative Q concurrent to negative q 85.6% of the time (cf. 85.3%) and positive Q concurrent to positive q 52.1% of the time (cf. 54.1%). Joint p.d.f.s of the eigenvalues of the strain-rate tensor against those from the reduced strain-rate tensor formed in the x_1 – x_3 plane were also found to be almost identical to figures 8 and 9 but are not shown for brevity.

Q and s_i , however, are scalars whereas in § 6 it is shown that the reduced VGT can also act as a predictor for the projection of the strain-rate eigenvectors onto the plane defining the reduced VGT. Figure 17 shows the p.d.f.s of the alignment cosines

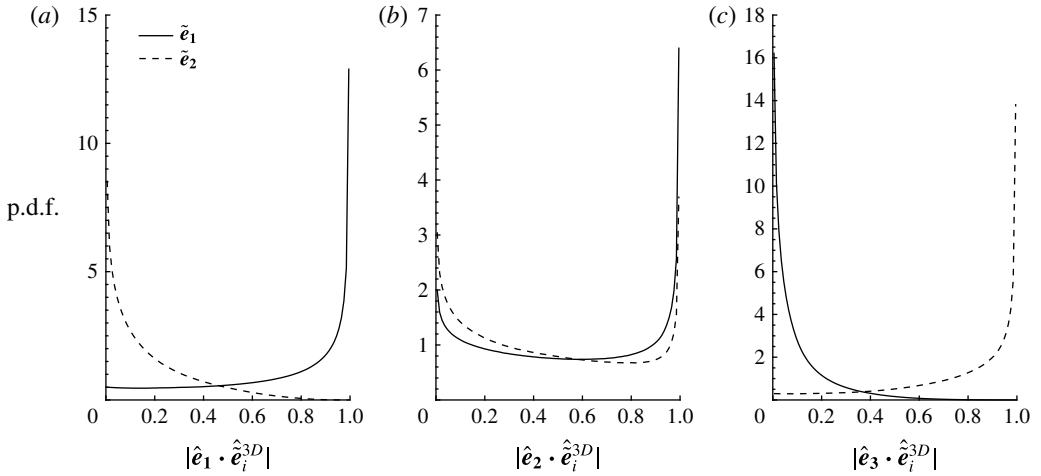


FIGURE 17. P.d.f.s of the alignment of the reduced strain-rate eigenvectors \tilde{e}_1 and \tilde{e}_2 in the x_1 - x_3 plane with the full strain-rate eigenvectors e_1 , e_2 and e_3 .

between the three-dimensional embedding of the eigenvectors of the reduced strain-rate tensor formed from data in the x_1 - x_3 plane and the strain-rate eigenvectors, similar to figure 14 for \tilde{S}_{ij} from the x_1 - x_2 plane. It is observed that the quantitative trends for the alignment tendencies of e_i with the reduced strain-rate eigenvectors in figures 14 and 17 are almost identical. It can thus be concluded that the reduced VGT is a good predictor of the behaviour of the fully three-dimensional strain-rate tensor in a shear flow, both in terms of vector and scalar quantities, without *a priori* knowledge as to the orientation of the mean strain. This provides evidence that the fine scales of the strain-rate tensor, at least, behave in a more locally isotropic manner than in a locally axisymmetric manner, reinforced by the near unity values of the isotropy parameters in §4.1. This observation further validates the approach that is taken in this manuscript of bounding S_{ij} from \tilde{S}_{ij} under the assumption of local isotropy and thus increases the confidence with which one may use the reduced VGT as an observable state of the full, three-dimensional VGT.

8. Conclusions

The reduced VGT (\tilde{A}_{ij}) is defined as a 2×2 block, from a single interrogation plane, of the full VGT. It has subsequently been shown in the study of Cardesa *et al.* (2013) that the joint p.d.f. of the invariants, p and q , for the characteristic equation for \tilde{A}_{ij} displays a characteristic ‘teapot’ shape for a number of turbulent flows. This distribution is confirmed in this study, lending credence to the notion that this shape is also a ‘universal’ feature of turbulent flows similar to the ‘teardrop’ shape for the joint p.d.f. between the second and third invariants of the full VGT.

The third invariant, R , of the VGT is comprised of the inviscid source/sink terms in the dynamics of strain rate (symmetric part of VGT) and rotation (skew-symmetric part of VGT), as emphasised in (1.2) and (1.3) respectively, and thus consists of sums of triple velocity gradient products. These terms are not present in two-dimensional turbulence and thus it is observed that the invariants of the reduced VGT are poor predictors of the kinematics of R , despite the fact that the ensemble average $\langle \omega_i S_{ij} \omega_j \rangle$

can be related to $\langle pq \rangle$ by (2.2). Contrastingly the second invariant Q reveals the local excess of rotation over strain rate, something that is described by two-dimensional turbulent phenomena. It is subsequently found that whilst the first invariant of \tilde{A}_{ij} , p , which effectively reveals the ‘compressibility’ of the reduced VGT is a poor predictor of Q , the second invariant, q , carries significant information on Q .

Further, it was observed that the ability to make predictions about the three-dimensional VGT from \tilde{A}_{ij} was significantly increased for straining regions of the flow ($Q < 0$) as opposed to swirling regions of the flow ($Q > 0$). This is evidenced by the greater variance of the joint p.d.f. between Q and q of figure 6 for $Q > 0$ and subsequent ability to predict the sign of Q based on q . This observation can be rationalised as follows: $Q > 0$ requires a dominance of rotation (skew-symmetric tensor) over strain rate (symmetric tensor). In three dimensions swirling is defined by a real and complex-conjugate pair of roots to the characteristic equation for A_{ij} , with the real eigenvector normal to the complex plane and defining the normal vector to the local swirling (Zhou *et al.* 1999). In two dimensions this real eigenvector cannot exist with only real or a complex-conjugate pair of roots being permissible for the characteristic equation for \tilde{A}_{ij} . To successfully describe swirling via the reduced VGT it is thus necessary to project this swirling eigenvector onto the two-dimensional plane from which the reduced VGT is formed. Whilst it is shown that the interrogation plane, that from which the reduced VGT is formed, is unimportant in the ability to predict the kinematics of both scalar quantities and vectors in three dimensions, the eigenframe of the strain-rate tensor will always have at least two vectors with a significant component in the interrogation plane. This is not necessarily the case for a single swirling eigenvector. Figure 15 shows that the special cases of \tilde{s}_1 and \tilde{s}_2 both having the same sign arise when there is a negligibly small component of e_1 or e_3 within the interrogation plane. There is evidently a higher likelihood of a single vector having a small component in the interrogation plane than an eigenframe of three vectors, hence the reduced ability of the reduced VGT to predict the full VGT in rotationally dominated regions of the flow.

Compared to the case of the full VGT, significantly more information can be derived about the strain-rate tensor S_{ij} from its reduced counterpart. A simple consequence of the fact that S_{ij} is symmetric implies that the full and reduced eigenvalues are ‘interlaced’ according to (3.3), meaning that knowledge of the reduced eigenvalues \tilde{s}_i restricts the location of the full eigenvalues s_i to certain intervals of the real line. If incompressibility is assumed, then stronger bounds can be placed upon the most extensive and compressive eigenvalues of S_{ij} , with these bounds implying that s_1 and s_3 lie in triangular cones in $(\tilde{s}_1, \tilde{s}_2, s_1)$ -space and $(\tilde{s}_1, \tilde{s}_2, s_3)$ -space, respectively. Furthermore, whilst it has been shown that $\langle s_2 \rangle > 0$ for turbulent flows (Ashurst *et al.* 1987; Tsinober *et al.* 1992; Lund & Rogers 1994), suggesting a mean tendency towards ‘sheet-forming’ topological evolution, $\langle s_2 \rangle < 0$ and hence preferential ‘tube-forming’ is observed for regions of the flow in which $\tilde{s}_1 < 0$.

Since the characteristic ‘teardrop’ shape of the p.d.f.s of Q and R is thought to be ‘universal’ for turbulent flows, it is not unreasonable to expect that simpler quantities such as the p.d.f.s of the reduced eigenvalues \tilde{s}_i enjoy a similar property. To begin to address this question, bounds have been derived upon the first two statistical moments of \tilde{s}_i , under the assumptions of isotropy and homogeneity. For example, the expected value $\langle \tilde{s}_1 \rangle$ must lie in a strictly positive interval, the lower end of which depends upon the kurtosis κ of $\partial u_1 / \partial x_1$, and tighter bounds are obtained for smaller values of κ . Whether this suggests that $\langle \tilde{s}_1 \rangle$ is itself dependent upon κ , or simply that the proven bound varies with κ , is an open question. Interestingly, the numerical data suggest that

the κ -independent bound on the upper end of the interval, proven by an application of the Cauchy–Schwarz inequality, is actually the most conservative.

Using the proven bounds for the expected values of \tilde{s}_i , bounds are also placed upon the variances and the covariance of the two eigenvalues. The covariance $\sigma(\tilde{s}_1, \tilde{s}_2)$ is shown to lie in the interval $[1/4((9/\kappa) - 5), 1/4]$ which appears conservative, since it is expected that $\sigma(\tilde{s}_1, \tilde{s}_2) < 0$ by virtue of the fact that $\tilde{s}_2 < 0 < \tilde{s}_1$ for over 85.2% of spatial locations. However, the upper bound of 1/4 may be lowered if a better upper bound can be found for $\langle \tilde{s}_1 \rangle$, again suggesting that attention should be focused upon improving this bound. Finally, we note that figure 13 suggests that \tilde{s}_1 is positively skewed, while \tilde{s}_2 is negatively skewed. Whether these properties can be inferred for isotropy and homogeneity presents an interesting question for future research.

Acknowledgement

The authors would like to acknowledge Dr S. Laizet for his role in the simulation of the dataset.

Appendix A

Suppose that $a, b > 0$ are constants such that

$$x^{1/2} \geq -ax^2 + bx, \quad x \geq 0. \tag{A 1}$$

Since $\langle X \rangle > 0$, it follows from substituting $y = x/\langle X \rangle$ into (A 1) that

$$y^{1/2} \geq \left(-a \frac{y^2}{\langle X \rangle^2} + \frac{b}{\langle X \rangle} y \right) \langle X \rangle^{1/2}, \quad y \geq 0. \tag{A 2}$$

Now, let f_X be the p.d.f. of the fluctuating variable X , which is assumed to be continuous. Then,

$$\begin{aligned} \langle X^{1/2} \rangle &= \int_0^\infty y^{1/2} f_X(y) dy \geq \left(-\frac{a}{\langle X \rangle^2} \int_0^\infty y^2 f_X(y) dy + \frac{b}{\langle X \rangle} \int_0^\infty y f_X(y) dy \right) \langle X \rangle^{1/2} \\ &= \left(-a \frac{\langle X^2 \rangle}{\langle X \rangle^2} + b \right) \langle X \rangle^{1/2} \end{aligned} \tag{A 3}$$

$$\text{(by (3.17))} = \left(b - \frac{2\kappa a}{3} \right) \langle X \rangle^{1/2}. \tag{A 4}$$

To maximize $(b - 2\kappa a/3)$ subject to the constraint (A 1), note first that (A 1) holds if and only if $ay^3 - by + 1 \geq 0$, for all $y \geq 0$. Elementary calculus can be used to show that this inequality holds if and only if

$$b \leq \left(\frac{4a}{27} \right)^{1/3}. \tag{A 5}$$

Since the objective $b - 2\kappa a/3$ is increasing in b , the optimal value is obtained when $b = (4a/27)^{1/3}$. Hence, the solution is given by the maximization problem

$$\max_{a>0} \left\{ \left(\frac{4a}{27} \right)^{1/3} - \frac{2\kappa a}{3} \right\} = \sqrt{\frac{3}{2\kappa}}. \tag{A 6}$$

REFERENCES

- ASHURST, W., KERSTEIN, A., KERR, R. & GIBSON, C. 1987 Alignment of vorticity and scalar gradient with strain rate in simulated Navier–Stokes turbulence. *Phys. Fluids* **30**, 2343–2353.
- BATCHELOR, G. K. 1946 The theory of axisymmetric turbulence. *Proc. R. Soc. Lond. A* **186**, 480–502.
- BATCHELOR, G. K. 1969 Computation of the energy spectrum in homogeneous two-dimensional turbulence. *Phys. Fluids* **12** (12), 233–239.
- BETCHOV, R. 1956 An inequality concerning the production of vorticity in isotropic turbulence. *J. Fluid Mech.* **1**, 497–504.
- BETCHOV, R. 1975 Numerical simulation of isotropic turbulence. *Phys. Fluids* **18** (10), 1230–1236.
- BISSET, D., HUNT, J. & ROGERS, M. 2002 The turbulent/non-turbulent interface bounding a far wake. *J. Fluid Mech.* **451**, 383–410.
- BUXTON, O. & GANAPATHISUBRAMANI, B. 2010 Amplification of enstrophy in the far field of an axisymmetric turbulent jet. *J. Fluid Mech.* **651**, 483–502.
- BUXTON, O., LAIZET, S. & GANAPATHISUBRAMANI, B. 2011a The effects of resolution and noise on kinematic features of fine-scale turbulence. *Exp. Fluids* **51** (5), 1417–1437.
- BUXTON, O., LAIZET, S. & GANAPATHISUBRAMANI, B. 2011b The interaction between strain-rate and rotation in shear flow turbulence from inertial range to dissipative length scales. *Phys. Fluids* **23**, 061704.
- CARDESA, J., MISTRY, D., GAN, L. & DAWSON, J. 2013 Invariants of the reduced velocity gradient tensor in turbulent flows. *J. Fluid Mech.* **716**, 597–615.
- CHANDRASEKHAR, S. 1950 The theory of axisymmetric turbulence. *Phil. Trans. R. Soc. Lond. A* **242**, 557–577.
- CHONG, M., PERRY, A. & CANTWELL, B. 1990 A general classification of three-dimensional flow fields. *Phys. Fluids A* **2** (5), 765–777.
- ELSINGA, G. & MARUSIC, I. 2010 Universal aspects of small-scale motions in turbulence. *J. Fluid Mech.* **662**, 514–539.
- ELSINGA, G., SCARANO, F., WIENEKE, B. & VAN OUDHEUSDEN, B. 2006 Tomographic particle image velocimetry. *Exp. Fluids* **41** (6), 933–947.
- FISCALETTI, D., WESTERWEL, J. & ELSINGA, G. E. 2014 Long-range μ PIV to resolve the small scales in a jet at high Reynolds number. *Exp. Fluids* **55** (9), 1–15.
- GEORGE, W. & HUSSEIN, H. 1991 Locally axisymmetric turbulence. *J. Fluid Mech.* **233**, 1–23.
- HIERRO, J. & DOPAZO, C. 2003 Fourth-order statistical moments of the velocity gradient tensor in homogeneous, isotropic turbulence. *Phys. Fluids* **15** (11), 3434–3442.
- HORN, R. & JOHNSON, C. 2013 *Matrix Analysis*. Cambridge University Press.
- JIMÉNEZ, J., WRAY, A., SAFFMAN, P. & ROGALLO, R. 1993 The structure of intense vorticity in isotropic turbulence. *J. Fluid Mech.* **255**, 65–90.
- LAIZET, S. & LAMBALLAIS, E. 2009 High-order compact schemes for incompressible flows: a simple and efficient method with quasi-spectral accuracy. *J. Comput. Phys.* **228** (16), 5989–6015.
- LAIZET, S., LARDEAU, S. & LAMBALLAIS, E. 2010 Direct numerical simulation of a mixing layer downstream a thick splitter plate. *Phys. Fluids* **22**, 015104.
- LUND, T. & ROGERS, M. 1994 An improved measure of strain state probability in turbulent flows. *Phys. Fluids* **6** (5), 1838–1847.
- MENEVEAU, C. 2011 Lagrangian dynamics and models of the velocity gradient tensor in turbulent flows. *Annu. Rev. Fluid Mech.* **43** (1), 219–245.
- MULLIN, J. & DAHM, W. 2006 Dual-plane stereo particle image velocimetry measurements of velocity gradient tensor fields in turbulent shear flow II. Experimental results. *Phys. Fluids* **18**, 035102.
- PERRY, A. & CHONG, M. 1987 A description of eddying motions and flow patterns using critical-point concepts. *Annu. Rev. Fluid Mech.* **19** (1), 125–155.
- PERRY, A. & CHONG, M. 1994 Topology of flow patterns in vortex motions and turbulence. *Appl. Sci. Res.* **53**, 357–374.
- DA SILVA, C. & PEREIRA, J. 2008 Invariants of the velocity-gradient, rate-of-strain, and rate-of-rotation tensors across the turbulent/non-turbulent interface in jets. *Phys. Fluids* **20** (055101).
- TANAHASHI, M., IWASE, S. & MIYAUCHI, T. 2001 Appearance and alignment with strain rate of coherent fine scale eddies in turbulent mixing layer. *J. Turbul.* **2** (N6), 1–17.

- TAYLOR, G. 1935 Statistical theory of turbulence. *Proc. R. Soc. Lond. A* **151** (873), 421–444.
- TAYLOR, G. 1938a Production and dissipation of vorticity in a turbulent fluid. *Proc. R. Soc. Lond. A* **164** (916), 15–23.
- TAYLOR, G. 1938b The spectrum of turbulence. *Proc. R. Soc. Lond. A* **164** (919), 476–490.
- TENNEKES, H. & LUMLEY, J. 1972 *A First Course in Turbulence*. MIT Press.
- TSINOBER, A. 2009 *An Informal Conceptual Introduction to Turbulence*, 2nd edn. Springer.
- TSINOBER, A., KIT, E. & DRACOS, T. 1992 Experimental investigation of the field of velocity gradients in turbulent flows. *J. Fluid Mech.* **242**, 169–192.
- TSINOBER, A., SHTILMAN, L. & VAISBURD, H. 1997 A study of properties of vortex stretching and enstrophy generation in numerical and laboratory turbulence. *Fluid Dyn. Res.* **21**, 477–494.
- VALENTE, P. C. & VASSILICOS, J. C. 2014 The non-equilibrium region of grid-generated decaying turbulence. *J. Fluid Mech.* **744**, 5–37.
- VAN ATTA, C. W. & ANTONIA, R. A. 1980 Reynolds number dependence of skewness and flatness factors of turbulent velocity derivatives. *Phys. Fluids* **23** (2), 252–257.
- VIILLEFOSSE, P. 1982 Local interaction between vorticity and shear in a perfect incompressible fluid. *J. Phys. (Paris)* **43** (6), 837–842.
- WINANT, C. & BROWAND, F. 1974 Vortex pairing: the mechanism of turbulent mixing-layer growth at moderate Reynolds number. *J. Fluid Mech.* **63**, 237–255.
- WYNGAARD, J. C. & TENNEKES, H. 1970 Measurements of the small-scale structure of turbulence at moderate Reynolds numbers. *Phys. Fluids* **13** (8), 1962–1969.
- ZHANG, J., TAO, B. & KATZ, J. 1997 Turbulent flow measurement in a square duct with hybrid holographic PIV. *Exp. Fluids* **23**, 373–381.
- ZHOU, J., ADRIAN, R., BALACHANDAR, S. & KENDALL, T. 1999 Mechanisms for generating coherent packets of hairpin vortices in channel flow. *J. Fluid Mech.* **387**, 353–396.